Soils and Seismology

Research Engineering

RESEARCH REPORT

CORRELATION OF PORE PRESSURE AND DISSIPATED ENERGY IN EARTHQUAKES – FIELD VERIFICATION

By

R.O. Davis and J.B. Berrill
Soils and Seismology
P.O. Box 29-336
Christchurch

March 2000

ENG 277

CORRELATION OF PORE PRESSURE AND DISSIPATED ENERGY IN EARTHQUAKES – FIELD VERIFICATION

Report prepared for the
Earthquake Commission Research Foundation

Project Number 99/340

By

R.O. Davis and J.B. Berrill
Soils and Seismology
P.O. Box 29-336
Christchurch

March 2000

PREFACE

This report describes work carried out under EQC Research Foundation Project 99/340: *Correlation of pore pressure and dissipated energy in earthquakes – Field verification*. The authors are grateful for the support of the Research Foundation as well as for assistance provided by international colleagues. In particular, thanks are expressed to Dr. Yoshinori Iwasaki and the Committee of Earthquake Observation and Research in the Kansai Area (CEORKA) for making the Kobe Port Island records available for this study. We are also grateful to Dr H.T. Tang of the Electric Power Research Institute for providing us with the Lotung records and to Professor Jiro Kuwano of Tokyo Institute of Technology and Professor Ikuo Towhata of the University of Tokyo for supplying digitised records from the Sunamachi test site. Finally we thank Professor R. Archuletta from the University of California, Santa Barbara, for providing the Elmore Ranch and Superstition Hills earthquake ground motion and pore pressure data.

ABSTRACT

The possibility of a correlation between dynamic pore pressure increase (*p*) and dissipated energy density (*D*) in soils subjected to earthquake shaking has been the subject of speculation for nearly twenty years. While cyclic loading tests have tended to confirm the *D-p* hypothesis in the laboratory, no field confirmation has been given. The research reported here focuses on field verification for the *D-p* hypothesis using existing acceleration and pore pressure recordings from downhole arrays. Downhole acceleration records from five different earthquakes are used to calculate continuous representations of shear stress and strain in the soils involved. These stress-strain records are then integrated to obtain time histories of dissipated energy density for comparison with measured pore pressure data. Remarkably good correlations of measured pore pressures with scaled energy profiles are found in most instances.

CONTENTS

1

INTRODUCTION

Records from downhole accelerometer arrays represent a valuable resource for geotechnical earthquake engineering. Most applications of downhole data are concerned with soft soil amplification of seismic waves but, in some downhole installations, pore pressure transducers have been used to record dynamic pore pressure increase simultaneously with acceleration measurement. In this report, records from four different downhole arrays, Kobe Port Island [1]*, Lotung, Taiwan [2], Sunamachi, near Tokyo [3] and the USGS Wildlife site in California [4], will be analysed. Our aim is to investigate the possible relationship between dissipated energy density and pore pressure increase in soils that may be potentially liquefiable. Unfortuantely, the Kobe Port Island array did not contain pore pressure transducers, but the other three sites did. Kobe is included in this study due to the fact liquefaction did occur there, and particularly complete acceleration data is available.

The possibility of a correlation between dynamic pore pressure increase (p) and dissipated energy density (D) in soils subjected to earthquake shaking has been the subject of speculation for nearly twenty years. Cyclic loading tests have tended to confirm the D-p hypothesis in the laboratory, but no field confirmation has yet been given. The first suggestion of a D-p relationship was by Nemmat-Nasser and Shokooh [5]. In their seminal work, a theoretical relationship linking D and p was proposed. Their idea was further developed by Davis and Berrill [6] and later by Berrill and Davis [7] in the context of liquefaction risk analysis. More recently, several investigators have considered the D-p hypothesis (Simcock, *et al.*, [8]; Law, *et al.*, [9]; Figueroa, *et al.*, [10]; Liang, *et al.*, [11]; Trifunic, [12]; Kayen and Mitchell, [13]). Some of these studies have involved laboratory experiments specifically designed to test the D-p concept in cyclic loading tests. Both dissipated energy and pore pressure have been simultaneously measured and the time histories compared. A fairly well defined D-p relationship has emerged from these tests. Recently, Davis and Berrill [14] have suggested a general procedure for pore pressure prediction in the field based on the D-p concept. Despite these developments, no field evidence for the relationship has yet been presented. The focus of this report is to provide field data from five earthquakes that lend support the D-p model.

The work reported below relies heavily on a method in which downhole acceleration records are used to synthesise shear stress and strain histories during an earthquake. We will use a recently formulated interpolation model [15] to continuously estimate shear stresses and strains at any depth based on measured accelerations from actual earthquakes at downhole array test sites. Our suggested interpolating functions are constructed in such a way that the free surface boundary condition will always be satisfied and the interpolated displacement and acceleration remain finite for all depths. We also show how the functions can be adapted to represent layered soil

* Numbers in square brackets refer to citations given at the end of the report

profiles. Depending on the number of instruments in the downhole array, a truncated series of interpolating functions can be derived so that each represents a modal shape for the layered soil profile. The resulting approximations for strain and stress are considered more accurate and robust than previous approximations. This is particularly important in relation to the present project, since dissipated energy is physically represented by the area enclosed within the stress-strain hysteresis loops that will be calculated.

Finally we can integrate the synthesised stress and strain to approximate the dissipated energy density in the test site soil at any depth of interest. A total of thirteen time histories of calculated pore pressure based on the *D-p* model will be presented and compared with measured excess pore pressures. The Kobe Port Island synthesised pore pressures are presented as well. In most cases reasonably good correlation between calculated and observed pore pressure time histories is found. In some of the cases the results are remarkably similar. Some differences are found in the case of the Superstition Hills earthquake, but the accuracy of the measured records from that event have been questioned by other researchers. The results presented below may shed further light on the validity of the Superstition Hills records.

2

ESTIMATION OF STRESS AND STRAIN

Prior to 1998 stress and strain estimates for downhole acceleration records [16] were based on simple linear interpolations. Consider the typical situation illustrated in Figure 1.

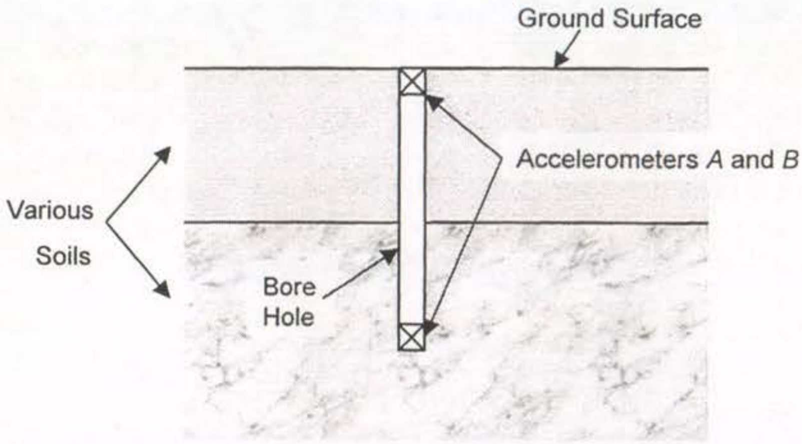

Figure 1. A typical downhole array with two accelerometers denoted *A* and *B*.

Suppose acceleration records a_A and a_B from two instruments denoted *A* and *B* have been obtained. These records are integrated to give the ground displacements u_A and u_B. All of the quantities a_A, a_B, u_A and u_B are functions of time. The usual approximations for stress τ and strain γ at any particular depth *x* and time *t* are

$$\tau(x,t) = \int_0^x \rho a(x,t)dx \approx \frac{\rho}{h_B - h_A}\left[(a_A h_B - a_B h_A)x + \frac{1}{2}(a_B - a_A)x^2\right]$$

$$\gamma(x,t) = \frac{\partial u(x,t)}{\partial x} \approx \frac{u_B - u_A}{h_B - h_A} \tag{1}$$

Here ρ denotes the soil density and h_A and h_B are the depths of the two instruments. Both approximations result from linear interpolation. In the case of the stress τ, the acceleration is interpolated between the two depths and then integrated. In the case of the strain γ, the displacement is interpolated and the slope measured. The accelerations a_A and a_B, and the displacements u_A and u_B, are evaluated at time *t*. If more than two instrument records are available, these representations might be altered somewhat, but the basic idea of linear interpolation would be retained.

An objection to approximations of the form given in (1) stems from the inability of linear interpolating functions to match the known boundary conditions for the problem. Regardless of specific site conditions, two things must always be true concerning the displacements and accelerations suffered by the site soils: (i) the ground surface must always be traction free and hence the spatial derivative of horizontal displacement at $x = 0$ must always be zero and (ii) the displacements must remain bounded as depth increases. These two boundary conditions are elementary, but neither can be satisfied by the linear interpolation models.

In this report we will synthesise stresses and strains using trigonometric interpolating functions, rather than linear, for both displacements and accelerations. The resulting approximations for stress and strain will automatically accommodate both the boundary conditions mentioned above. An additional advantage will also become apparent. We will derive a relatively simple model for layered site response, and it will be used to adjust the calculations for stress and strain in an appropriate way. In this section the equations used for interpolation as well as for synthesis of stress and strain will be developed. It will be convenient to illustrate the method by analysing a specific set of downhole records. The Port Island record from the Kobe earthquake will be used for this purpose.

Analysis for Homogeneous Soil

While it is possible to consider layered soils, the development for a homogeneous site is simpler and will illustrate the central points of our method. Here we consider a homogeneous soil profile in which a downhole accelerometer array has been placed. Let the instruments be denoted *A, B, ..., J* in order of increasing depths $h_A, h_B, \ldots$ h_J.

Also let $u(x,t)$ denote horizontal displacement and $\ddot{u}(x,t)$ horizontal acceleration in the particular orientation of the instrumental record with which we are concerned. We will identify the specific acceleration at instrument λ by a_λ, $\lambda = A, B, \ldots, J$. The corresponding displacement will be u_λ.

At any particular depth *h* the shear strain and stress are given by

$$\gamma(h,t) = \frac{\partial u(h,t)}{\partial x}$$

$$\tau(h,t) = \int_0^h \rho \ddot{u}(x,t) dx \qquad (2)$$

We will use equations (2) together with appropriate interpolation functions for displacement and acceleration to solve for the strain and stress at any particular time *t*.

A variety of interpolation functions are available to us. While linear interpolation possesses the advantage of simplicity, the free surface boundary condition can never be satisfied, hence we discard it. Polynomials of degree two or higher do have the ability to satisfy the boundary condition at $x = 0$, but they will generally become unbounded as x increases. A third possibility, and the one we employ here, is a trigonometric series. In particular, a cosine series will automatically satisfy the free surface boundary condition and will remain finite as $x \to \infty$. Thus we introduce the following interpolating functions for displacement and acceleration.

$$
\begin{aligned}
u(x,t) &= \beta_o + \beta_1 \cos\kappa x + \beta_2 \cos 2\kappa x + \cdots + \beta_{J-1}\cos(J-1)\kappa x \\
\ddot{u}(x,t) &= \alpha_1 \cos\kappa x + \alpha_2 \cos 2\kappa x + \cdots + \alpha_J \cos J\kappa x
\end{aligned}
\tag{3}
$$

The number of terms for each series is J, the number of downhole instruments. The coefficients $\alpha_\lambda, \beta_\lambda$ are functions of time. They will be determined by the instantaneous values of measured displacement and acceleration. The inclusion of the coefficient β_o in the displacement expansion where no similar term appears in the acceleration series occurs for reasons to be explained below. Note the presence of one additional arbitrary constant, the wave number κ. We will suggest an appropriate range of values for κ shortly.

Determination of the coefficients in (3) is a straightforward matter. To illustrate this, consider the acceleration series. To determine the coefficients α_λ we have the following set of J equations.

$$
\begin{bmatrix} c_{1A} & c_{2A} & \cdots & c_{JA} \\ c_{1B} & c_{2B} & \cdots & c_{JB} \\ \vdots & & & \\ c_{1J} & c_{2J} & \cdots & c_{JJ} \end{bmatrix}
\begin{bmatrix} \alpha_1 \\ \alpha_2 \\ \vdots \\ \alpha_J \end{bmatrix}
=
\begin{bmatrix} a_A \\ a_B \\ \vdots \\ a_J \end{bmatrix}
\tag{4}
$$

Here

$$
c_{\lambda N} = \cos\lambda\kappa h_N \ , \qquad \lambda, N = 1,2,\cdots,J \tag{5}
$$

It is a simple matter to solve (4) for the vector of coefficients α_λ. Having done so, the shear stress at any depth h is obtained from (2). Carrying out the integration we find

$$
\tau(h,t) = \frac{\rho}{\kappa}\left[\alpha_1 \sin\kappa h + \frac{1}{2}\alpha_2 \sin 2\kappa h + \cdots + \frac{1}{J}\alpha_J \sin J\kappa h\right] \tag{6}
$$

A similar development for strain gives

$$
\gamma(h,t) = -\kappa\left[\beta_1 \sin\kappa h + 2\beta_2 \sin 2\kappa h + \cdots + (J-1)\beta_{J-1}\sin(J-1)\kappa x\right] \tag{7}
$$

where the coefficients β_λ are determined by an equation similar to (4) with a vector of measured displacements instead of accelerations.

Before ending the discussion for homogeneous sites, we will discuss one other detail. Following equation (3) we noted that the strain approximation contained a constant term β_o while no equivalent term is found in the stress approximation. The reason for this is to ensure the strain approximation will approach zero for a rigid body deformation. We can illustrate this point by considering how the approximation works in the simple case of harmonic excitation of a linearly elastic soil column. For vertically propagating harmonic SH waves, the horizontal displacement $u(x,t)$ is given by

$$u(x,t) = u_o(e^{ikx} + e^{-ikx})e^{i\omega t} \tag{8}$$

Here u_o denotes the wave amplitude, ω is the circular frequency of excitation, and k is the excitation wave number (not to be confused with the approximation wave number κ), given by

$$k = \frac{\omega}{c} \tag{9}$$

where c denotes the shear wave velocity. Equation (8) satisfies both the equation of motion and the free surface boundary condition at $x = 0$. The two exponentials inside the brackets represent upward and downward propagating waves. Both waves must have the same amplitude because of the free surface boundary condition. It will be more convenient to rewrite equation (8) as

$$u(x,t) = 2u_o \cos kx e^{i\omega t} \tag{10}$$

Now suppose we have a two-instrument array subject to the motion specified in (10). The strain approximation is easily found from equation (7)

$$\gamma(h,t) = \frac{-\kappa \sin \kappa h (u_B - u_A)}{(c_{1B} - c_{1A})} \tag{11}$$

where u_A and u_B are obtained from (10) with x set equal to h_A and h_B. In the limit as $\omega \to 0$, we have $u_A \to u_B$, and hence $\gamma \to 0$, the expected result for rigid translation. If, on the other hand, the constant coefficient β_0 had not been used in equation (3), then (11) would be replaced by

$$\gamma(h,t) = \frac{-\kappa\left[(c_{2B}u_A - c_{2A}u_B)\sin \kappa h + (c_{1A}u_B - c_{1B}u_A)\sin 2\kappa h\right]}{c_{1A}c_{2B} - c_{1B}c_{2A}}$$

Now, in the limit as $\omega \to 0$, we find γ will not, in general, vanish. Clearly (11) is the better approximation based on behaviour for low frequency excitation. A similar problem does not arise for the acceleration approximation since, in the zero frequency limit, the elastic accelerations all go to zero.

Example: Kobe Earthquake

To illustrate our ideas we will consider the ground motion measurements obtained in the Port Island downhole array from the Kobe earthquake [1]. In this section we treat the Port Island soil profile as though it were homogeneous. Later the effects of soil layering will be considered. A central concern in this section will be selection of appropriate values for the approximation wave number κ.

The downhole array at Port Island consisted of four three-component accelerometers at depths 0 *m*, 16 *m*, 32 *m*, and 83 *m*. Figure 2 shows the recorded accelerations for the East-West component. The full 60-second record is shown.

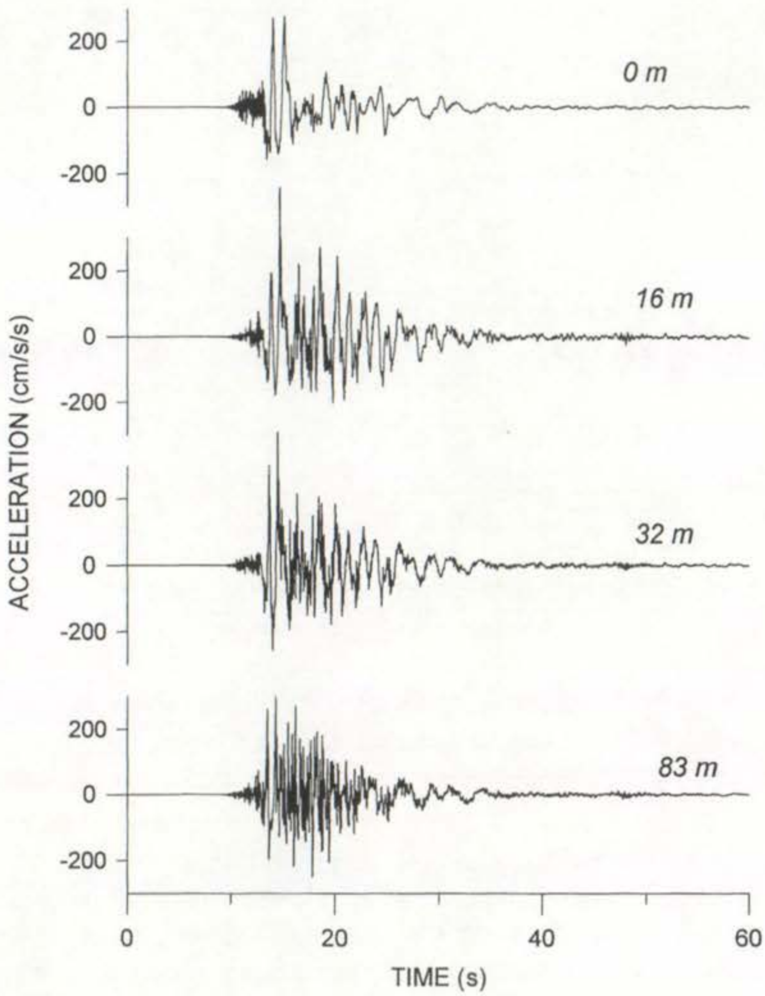

Figure 2. East-West accelerations from the Kobe Port Island downhole array.

It is clear from this figure that the strongest motion for this earthquake occurred over a relatively short time period. This is particularly true at the ground surface where liquefaction effects have filtered the higher frequency excitation propagating upward through the Port Island soil column. Figure 3 shows an enlarged view of the accelerations between roughly 12 and 24 seconds together with the integrated displacement time histories. We will focus attention on the first major acceleration pulse which occurs roughly between 13.5 and 14.5 seconds on this record.

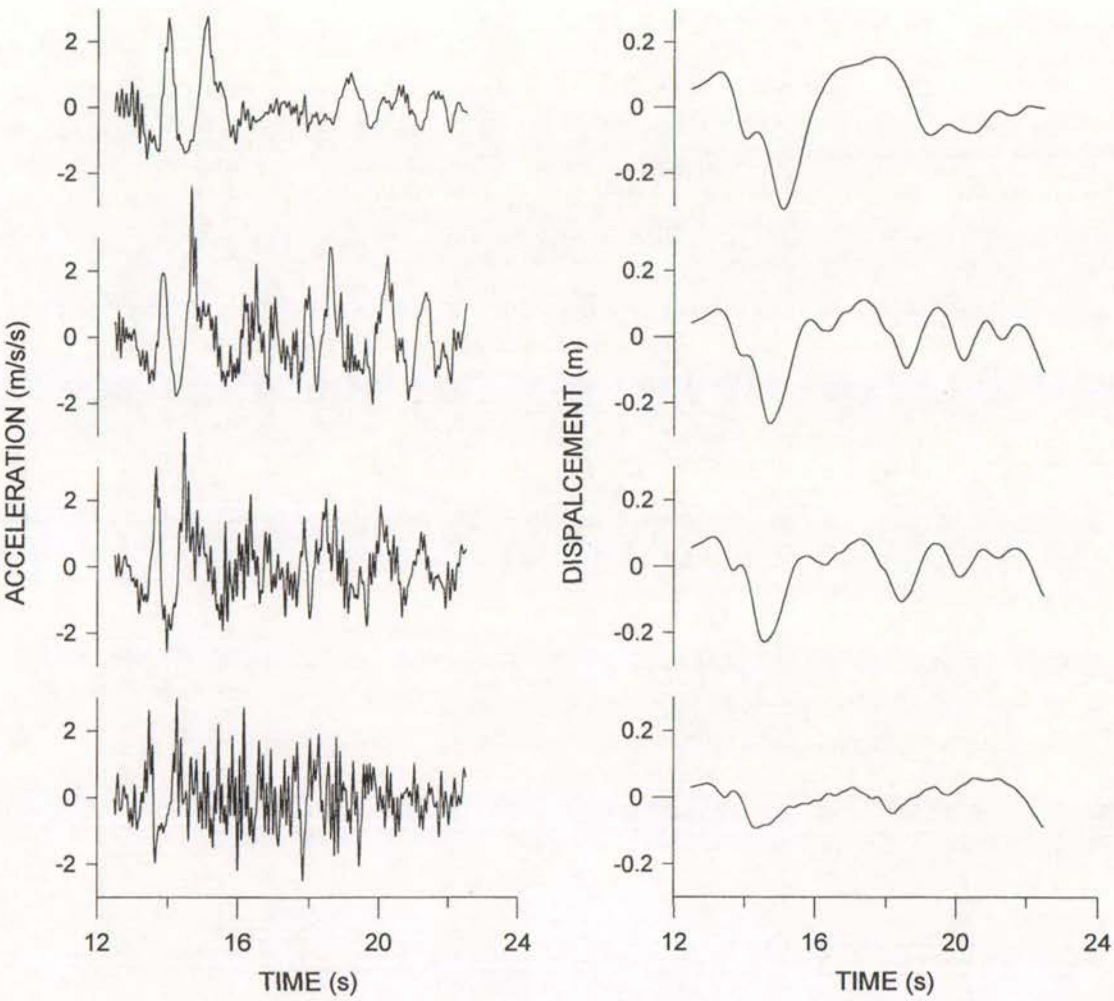

Figure 3. Expanded view of East-West accelerations from Kobe Port Island together with integrated displacements.

To begin we have shown in Figure 4 graphs of stress versus strain at two depths, 12 *m* and 23 *m*, obtained from equations (6) and (7) and based on all four downhole records. The illustrated calculations were carried out with a value of 0.02 m^{-1} for the wave number κ. In selecting this value for κ we are mindful that the most accurate approximation we can hope for can only represent that part of the input wave spectrum with wave lengths on the order of the spacing between downhole instruments or longer. High frequency, short length waves cannot be approximated by an array of widely spaced instruments, just as the Nyquist frequency limits the analysis high frequency time series data. Since the wave number is 2π times the reciprocal of wave length, these comments suggest we use a small value for κ corresponding to a long wave length. It should not be too small however, else there will be no advantage in using the cosine series. Because of these reasons, we suggest a two-step procedure for selection of κ. We first choose a trial value for κ based on the greatest instrument depth being roughly a quarter wave length. That is

$$\kappa = \frac{2\pi}{4\left(h_D - h_A\right)} = \frac{\pi}{2 \times 83} \approx 0.02\ m^{-1} \qquad (12)$$

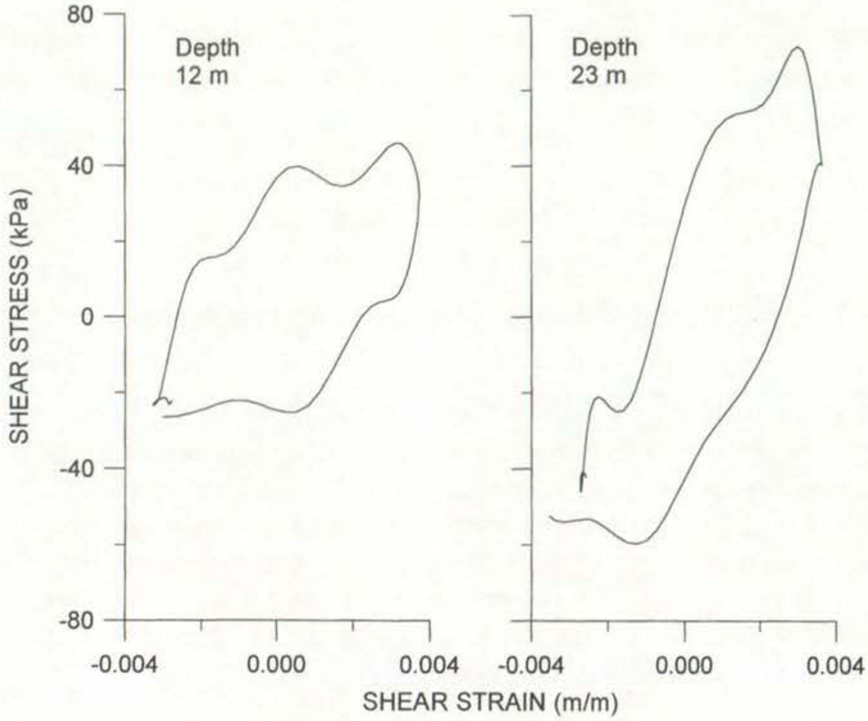

Figure 4. Stress – strain response at two depths based on Port Island records

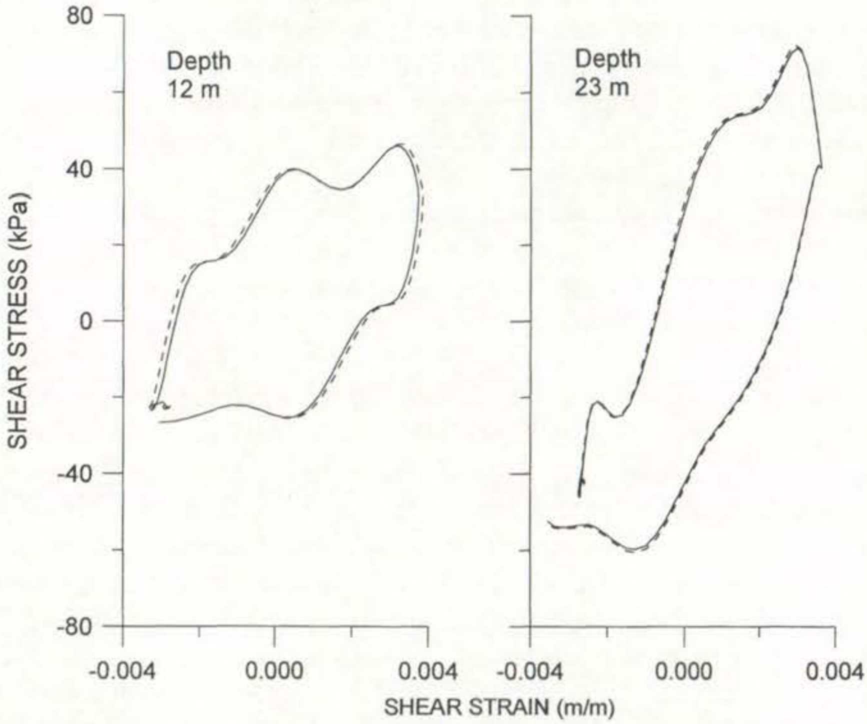

Figure 5. Comparison of approximated stress – strain response for values of the approximation wave number κ equal to $0.005\,m^{-1}$ (dashed line) and $0.02\,m^{-1}$ (solid line).

The second step compares $J\kappa$ with what we will refer to as the Nyquist wave number, namely 2π divided by twice the smallest instrument spacing. For the Port Island array the Nyquist wave number is

$$\kappa_N = \frac{2\pi}{2(h_B - h_A)} = \frac{\pi}{16} \approx 0.20m^{-1}$$

If the value of $J\kappa$ is smaller than κ_N, we accept the trial value for κ; otherwise, we reduce κ to some value smaller than κ_N / J. For the Port Island array we have $J\kappa = 4 \times 0.02 = 0.08m^{-1} < \kappa_N$, hence the original trial value is acceptable. This procedure is based on the idea that the interpolating cosine series can be looked upon as an expansion of eigenfunctions representing the modes of shearing vibration for a homogeneous soil layer with depth equal to the greatest instrument spacing. The first term, with wave number κ, represents the fundamental mode, while the higher terms represent higher modes. The wave number of the highest mode, $J\kappa$, should not exceed the Nyquist wave number in order to avoid spurious information being introduced by the interpolating functions.

What will be the effect if we change κ? Making κ smaller appears to have relatively minor effects as is shown in Figure 5 where similar calculations of stress and strain are illustrated for $\kappa = 0.005\ m^{-1}$ (dashed line) and $\kappa = 0.02\ m^{-1}$ (solid line). We have effectively tripled the approximation wave length, but the change in both the stress and strain approximations appears small. In fact the approximations are more different than first appears as illustrated in Figure 6 where the interpolated displacement profiles for the two cases are graphed. These profiles correspond to a time of 14.0 seconds on the instrumental records, the time at which the maximum stress is attained at the 0 *m* depth. The '+' signs mark the measured values of displacement from the downhole instruments. While the two calculations are similar in the upper 32 *m*, they differ markedly at greater depths. This figure clearly demonstrates the lack of control over the approximated displacements when the instruments are more widely dispersed.

Clearly the stress and strain approximations will be sensitive to the value chosen for κ. The displacement profiles of Figure 6 represent conditions at only one time in the recordings, but the same general conclusions apply for literally any other time. Selection of κ is a matter of judgement, although the form given in equation (12) has been found to work well throughout the calculations done for this report. Use of a larger value for κ than that specified by (12) can lead to the introduction of short wave length information into the approximations where it is not justified by the measured data. This point is discussed in Davis and Berrill [15]. The development here also emphasises the importance of the instrument spacing in a downhole array. Widely spaced instruments will not in general yield useful approximations for stress and strain, regardless of what level of sophistication is employed in their analysis.

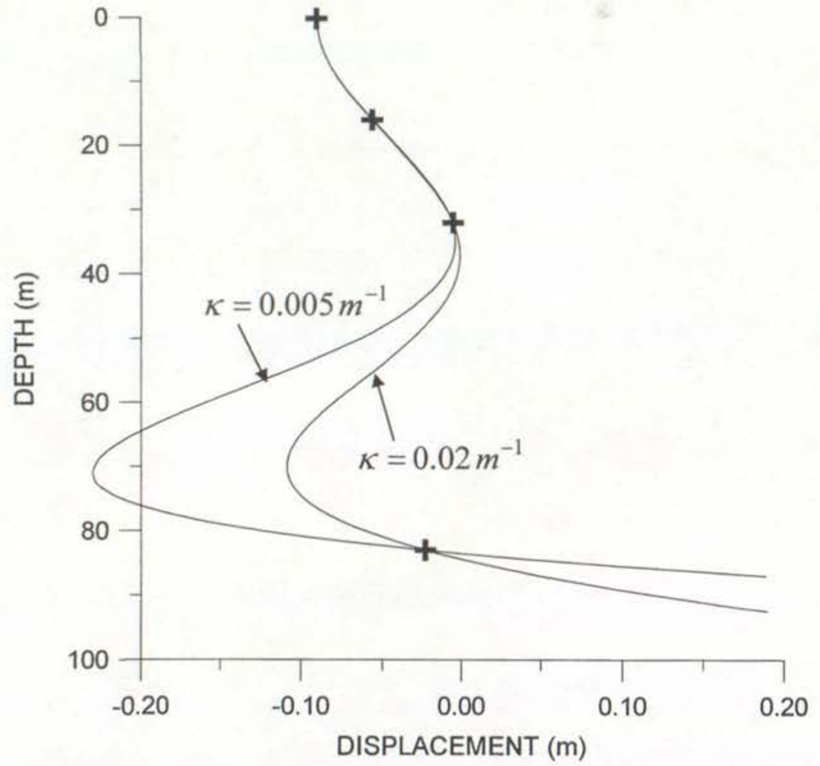

Figure 6. Profiles of interpolated displacement versus depth for two values of κ. The + signs denote the four measured displacements.

Analysis for Layered Soils

The full power embedded in the cosine series approximation does not become evident until we consider a layered soil site. Let the soil profile be as indicated in Figure 7. We see a sequence of horizontal layers numbered downward from the ground surface. The thickness of layer *m* is denoted h_m and the density and shear wave velocity of the layer are given by ρ_m and c_m. As will be seen shortly, it is not necessary to know in advance the value of c_m, but it will be necessary to estimate the impedance ratios $\rho_m c_m / \rho_n c_n$ for all layers before solving for stresses and strains.

We begin by constructing a local coordinate frame for layer *m*. The depth *h* is measured from the upper surface of the layer as shown in Figure 7. In order to analyse the layered soil problem, it will be useful to consider harmonic waves propagating vertically in the soil profile. For any given frequency, this is equivalent to considering the Fourier components of a more general wave form. Let u_m and τ_m denote the Fourier components of displacement and shear stress for frequency $\lambda\omega$ evaluated at the upper surface of the layer. The corresponding displacement and stress at depth *h* are given by

$$\begin{Bmatrix} u(h,t,m) \\ \tau(h,t,m) \end{Bmatrix} = \left[\mathbf{H}_m\right] \begin{Bmatrix} u_m \\ \tau_m \end{Bmatrix} \tag{13}$$

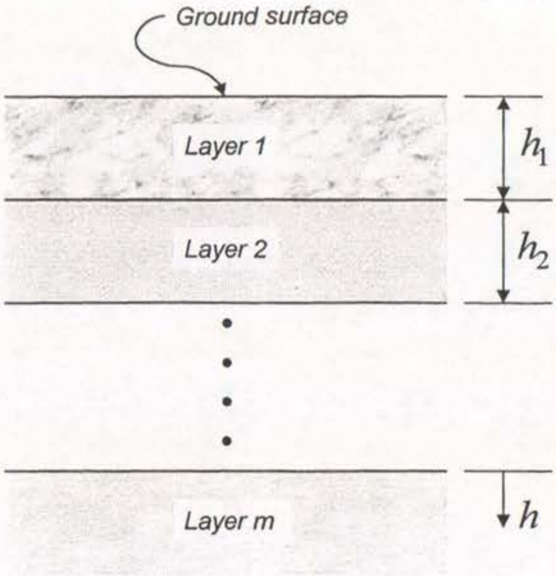

Figure 7. Typical layered soil profile

In equation (13) $\mathbf{H}_m$ represents the Haskell-Thomson transfer matrix [17]

$$\mathbf{H}_m = \begin{bmatrix} \cos \lambda \kappa_m h & \dfrac{1}{\lambda \omega \rho_m c_m} \sin \lambda \kappa_m h \\ -\lambda \omega \rho_m c_m \sin \lambda \kappa_m h & \cos \lambda \kappa_m h \end{bmatrix} \tag{14}$$

and the wave number κ_m is given by

$$\kappa_m = \omega / c_m \ .$$

Shortly we will let λ take on values 0, 1, 2 .... giving a discrete sequence of frequencies from which expressions similar to those in equation (3) can be constructed. Note the explicit dependence on layer m shown on the left side of equation (13).

In the special case of the uppermost layer ($m = 1$), equation (13) gives

$$u(h,t,1) = u_1 \cos \lambda \kappa_1 h \ , \quad 0 \le h \le h_1 \tag{15}$$

Here u_1 denotes the Fourier component of displacement at the ground surface and we have used the zero stress boundary condition $\tau_1 = 0$. In the analysis below we will interpret the displacement u_1 as a coefficient β_λ of one of the terms in a series similar to the cosine series for displacement in equation (3).

The most useful aspect of the transfer matrix is that we can multiply matrices for successive layers to obtain the displacement at any point in the soil profile. That is, we can rewrite (13) as product of m matrices

$$\begin{Bmatrix} u(h,t,m) \\ \tau(h,t,m) \end{Bmatrix} = \left[\mathbf{H}_m\right]\left[\mathbf{H}_{m-1}\right]\cdots\left[\mathbf{H}_1\right]\begin{Bmatrix} u_1 \\ 0 \end{Bmatrix} \tag{16}$$

This equation relates the displacement and shear stress in layer m to the displacement and the *zero* shear stress at the ground surface. The matrices $\mathbf{H}_{m-1}$, $\mathbf{H}_{m-2}$, ... ,$\mathbf{H}_1$ are evaluated with h equal to the appropriate layer thickness $h_{m-1}, h_{m-2}, \cdots, h_1$. In the matrix $\mathbf{H}_m$, of course, h can take on any value between 0 and h_m. Now we can easily use (16) to build up the displacement in any layer. For example, in layer 2 we have

$$u(h,t,2) = u_1 \cos\lambda\kappa_1 h_1 \cos\lambda\kappa_2 h - u_1 \frac{\rho_1 c_1}{\rho_2 c_2} \sin\lambda\kappa_1 h_1 \sin\lambda\kappa_2 h, \quad 0 \le h \le h_2 \tag{17}$$

while in layer 3

$$\begin{aligned} u(h,t,3) = {} & u_1 \cos\lambda\kappa_1 h_1 \cos\lambda\kappa_2 h_2 \cos\lambda\kappa_3 h \\ & - u_1 \frac{\rho_1 c_1}{\rho_2 c_2} \sin\lambda\kappa_1 h_1 \sin\lambda\kappa_2 h_2 \cos\lambda\kappa_3 h \\ & - u_1 \frac{\rho_2 c_2}{\rho_3 c_3} \cos\lambda\kappa_1 h_1 \sin\lambda\kappa_2 h_2 \sin\lambda\kappa_3 h \\ & - u_1 \frac{\rho_1 c_1}{\rho_3 c_3} \sin\lambda\kappa_1 h_1 \cos\lambda\kappa_2 h_2 \sin\lambda\kappa_3 h \end{aligned} \tag{18}$$

The entire displacement profile can be constructed in this manner moving down through each layer successively. Note that in each of the expressions above h is measured from the upper surface of the relevant layer.

Next, fix the value of the frequency ω and consider the expressions above as λ takes on values 0, 1, 2, ... Let $c^m_{\lambda h}$ represent the combination of terms that multiply u_1 in the expression for the displacement $u(h,t,m)$. That is, for $m = 1$,

$$c^1_{\lambda h} = \cos\lambda\kappa_1 h \quad , \quad \kappa_1 = \omega/c_1 \tag{19}$$

which follows from (15). Similarly, for $m = 2$, we have from (17)

$$c^2_{\lambda h} = \cos\lambda\kappa_1 h_1 \cos\lambda\kappa_2 h - \frac{\rho_1 c_1}{\rho_2 c_2} \sin\lambda\kappa_1 h_1 \sin\lambda\kappa_2 h \quad , \quad \kappa_m = \omega/c_m \tag{20}$$

Then we can approximate the entire displacement profile with a series of the form

$$u(h,t,m) = \beta_0 + \beta_1 c^m_{1h} + \beta_2 c^m_{2h} + \cdots \tag{21}$$

where the coefficients β_0, β_1, $\beta_2, \ldots$ will be determined by the measured displacements from the downhole instrument records. We can look upon each of the functions $c_{\lambda h}^{m}$ as a modal shape. The coefficients β_λ are weightings that physically represent the ground surface displacement u_1 corresponding to each mode.

Now suppose one instrument of a downhole array lies in layer m. Let the instrument be identified by A and let h_A denote the position of the instrument in the layer measured from the layer surface. Then let $c_{\lambda A}^{m}$ represent the function $c_{\lambda h}^{m}$ with h replaced by h_A so that

$$u_A = u(h_A, t, m) = u_1 c_{\lambda A}^{m} \tag{22}$$

where we have used u_A to represent the measured value at time t from the downhole array. Next, suppose we have an array of instruments A, B, ..., J placed in soil layers $m_A, m_B, \cdots, m_J$. Then we can approximate the complete displacement field with a truncated series of the form

$$u(h,t,m) = \beta_0 + \beta_1 c_{1h}^{m} + \beta_2 c_{2h}^{m} + \cdots + \beta_{J-1} c_{(J-1)h}^{m} \tag{23}$$

where the coefficients β_λ are determined by solving this set of equations

$$\begin{bmatrix} 1 & c_{1A}^{m_A} & c_{2A}^{m_A} \cdots & c_{(J-1)A}^{m_A} \\ 1 & c_{1B}^{mB} & c_{2B}^{m_B} \cdots & c_{(J-1)B}^{m_B} \\ \vdots & & & \\ 1 & c_{1J}^{m_J} & c_{2J}^{m_J} \cdots & c_{(J-1)J}^{m_J} \end{bmatrix} \begin{Bmatrix} \beta_0 \\ \beta_1 \\ \vdots \\ \beta_{J-1} \end{Bmatrix} = \begin{Bmatrix} u_A \\ u_B \\ \vdots \\ u_J \end{Bmatrix} \tag{24}$$

Once the coefficients β_λ have been determined for a particular value of t, the strain at any depth h in any layer m immediately follows from

$$\gamma(h,t,m) = \left[\frac{\partial u(x,t,m)}{\partial x}\right]_{x=h} = \left[\beta_1 \frac{\partial c_{1h}^{m}}{\partial x} + \beta_2 \frac{\partial c_{2h}^{m}}{\partial x} + \cdots + \beta_{J-1} \frac{\partial c_{(J-1)h}^{m}}{\partial x}\right]_{x=h} \tag{25}$$

To illustrate this, suppose we have a situation with three downhole instruments. For any particular time t we use equation (24) to find the coefficients β_λ. Then for a point in layer 1 we have the simple result

$$\gamma(h,t,1) = -\beta_1 \kappa_1 \sin\kappa_1 h - 2\beta_2 \kappa_1 \sin 2\kappa_1 h \tag{26}$$

and this equation applies for $0 \le h \le h_1$. In layer 2 we have

$$\begin{aligned} \gamma(h,t,2) = &-\beta_1 \kappa_2 \left(\cos\kappa_1 h_1 \sin\kappa_2 h + \frac{\rho_1 c_1}{\rho_2 c_2} \sin\kappa_1 h_1 \cos\kappa_2 h\right) \\ &- 2\beta_2 \kappa_2 \left(\cos 2\kappa_1 h_1 \sin 2\kappa_2 h + \frac{\rho_1 c_1}{\rho_2 c_2} \sin 2\kappa_1 h_1 \cos 2\kappa_2 h\right) \end{aligned} \tag{27}$$

which applies for $0 \le h \le h_2$. Similar expressions are easily obtained for layers 3, 4, etc.

We can follow a parallel development to find the shear stress. First we need to approximate the acceleration profile in the layered soil. This can be done with a transfer matrix approach similar to (13). Focusing on accelerations, the appropriate equation for layer m involves acceleration and stress

$$\begin{Bmatrix} \ddot{u}(h,t,m) \\ \tau(h,t,m) \end{Bmatrix} = \left[\mathbf{L}_m\right] \begin{Bmatrix} \ddot{u}_m \\ \tau_m \end{Bmatrix} \tag{28}$$

where the transfer matrix $\mathbf{L}_m$ is given by

$$\mathbf{L}_m = \begin{bmatrix} \cos\lambda\kappa_m h & -\dfrac{\lambda^2\omega^2}{\rho_m c_m}\sin\lambda\kappa_m h \\ (\lambda\omega)^{-2}\rho_m c_m \sin\lambda\kappa_m h & \cos\lambda\kappa_m h \end{bmatrix} \tag{29}$$

As before, we can multiply successive transfer matrices in order to relate the acceleration in layer m to that at the ground surface.

$$\begin{Bmatrix} \ddot{u}(h,t,m) \\ \tau(h,t,m) \end{Bmatrix} = \left[\mathbf{L}_m\right]\left[\mathbf{L}_{m-1}\right]\cdots\left[\mathbf{L}_1\right] \begin{Bmatrix} \ddot{u}_1 \\ 0 \end{Bmatrix} \tag{30}$$

Then in layer 1 the acceleration is

$$\ddot{u}(h,t,1) = \ddot{u}_1 \cos\lambda\kappa_1 h\,, \qquad 0 \le h \le h_1 \tag{31}$$

while in layer 2

$$\ddot{u}(h,t,2) = \ddot{u}_1 \cos\lambda\kappa_1 h_1 \cos\lambda\kappa_2 h - \ddot{u}_1 \frac{\rho_1 c_1}{\rho_2 c_2}\sin\lambda\kappa_1 h_1 \sin\lambda\kappa_2 h, \quad 0 \le h \le h_2 \tag{32}$$

An equation similar to (18) occurs for layer 3. Note that the collection of terms that multiply the surface acceleration $\ddot{u}_1$ are the same as the coefficients $c^m_{\lambda h}$ which arose in the development for displacements.

Now we can approximate the complete acceleration profile with a series similar to equation (23)

$$\ddot{u}(h,t,m) = \alpha_1 c^m_{1h} + \alpha_2 c^m_{2h} + \cdots + \alpha_{J-1} c^m_{(J-1)h} \tag{33}$$

where the coefficients α_λ are obtained from the measured accelerations by solving

$$\begin{bmatrix} c_{1A}^{m_A} & c_{2A}^{m_A} \cdots c_{(J-1)A}^{m_A} \\ c_{1B}^{mB} & c_{2B}^{m_B} \cdots c_{(J-1)B}^{m_B} \\ \vdots & \\ c_{1J}^{m_J} & c_{2J}^{m_J} \cdots c_{(J-1)J}^{m_J} \end{bmatrix} \begin{Bmatrix} \alpha_1 \\ \alpha_2 \\ \vdots \\ \alpha_{J-1} \end{Bmatrix} = \begin{Bmatrix} a_A \\ a_B \\ \vdots \\ a_J \end{Bmatrix} \tag{34}$$

Note that no constant term α_0 is required here.

Finally we obtain the shear stress by integrating the accelerations. A separate integral is required for each layer.

$$\tau(h,t,m) = \int_0^{h_1} \rho_1\, \ddot{u}(x,t,1)dx + \int_0^{h_2} \rho_2\, \ddot{u}(x,t,2)dx + \cdots + \int_0^{h} \rho_m\, \ddot{u}(x,t,m)dx \tag{35}$$

Once again suppose three downhole records are available. Then for a particular time t we can determine the coefficients α_1, α_2, α_3 from equation (34). The stress in layer 1 will be given by

$$\tau(h,t,1) = \frac{\rho_1}{\kappa_1}\left(\alpha_1 \sin\kappa_1 h + \frac{\alpha_2}{2}\sin 2\kappa_1 h + \frac{\alpha_3}{3}\sin 3\kappa_1 h \right) \tag{36}$$

In layer 2 we have

$$\begin{aligned} \tau(h,t,2) = {} & \frac{\rho_1}{\kappa_1}\left(\alpha_1 \sin\kappa_1 h_1 + \frac{\alpha_2}{2}\sin 2\kappa_1 h_1 + \frac{\alpha_3}{3}\sin 3\kappa_1 h_1 \right) \\ & + \frac{\rho_2\alpha_1}{\kappa_2}\left(\cos\kappa_1 h_1 \sin\kappa_2 h - \frac{\rho_1 c_1}{\rho_2 c_2}\sin\kappa_1 h_1 \left[1-\cos\kappa_2 h\right] \right) \\ & + \frac{\rho_2\alpha_2}{2\kappa_2}\left(\cos 2\kappa_1 h_1 \sin 2\kappa_2 h - \frac{\rho_1 c_1}{\rho_2 c_2}\sin 2\kappa_1 h_1 \left[1-\cos 2\kappa_2 h\right] \right) \\ & + \frac{\rho_2\alpha_3}{3\kappa_2}\left(\cos 3\kappa_1 h_1 \sin 3\kappa_2 h - \frac{\rho_1 c_1}{\rho_2 c_2}\sin 3\kappa_1 h_1 \left[1-\cos 3\kappa_2 h\right] \right) \end{aligned} \tag{37}$$

Expressions for subsequent layers become longer but no additional real difficulties arise.

We can use equations (25) and (35) to estimate the stress and strain in the layered soil at any particular time t. In comparison to the homogeneous soil case, some additional information is required concerning the various soils. Naturally an estimate for the density of each layer ρ_m is needed. The model is not particularly sensitive to ρ_m and in many instances a constant value for all layers would probably be sufficient. More important are the values for the impedance ratios $\rho_m c_m / \rho_n c_n$ between the various layers. These values must be specified in advance and they play an important role in determining the modal shapes $c_{\lambda h}^{m}$ in all layers below the uppermost layer. It is not necessary to specify the stiffness or the shear wave velocity for any individual layer.

We must select an appropriate value for one of the wave numbers κ_λ depending on the depth at which the stress and strain approximations are desired and the spacing of instruments. The other wave numbers then follow from the impedance ratios and the assumed densities. The layered model appears to be moderately insensitive to the values of the wave numbers (as was the case for the homogeneous model) provided reasonable values are used. Aside from these points the only other information needed is values for the thickness of each layer. Naturally, as the number of layers increases, so will the amount of algebra, but the equations are easily handled by machine.

3

PORE PRESSURE – DISSIPATED ENERGY RELATIONSHIPS

In the next section we will attempt to model the measured pore pressure rise at four different test sites using a relationship between pore pressure and dissipated energy density. Nemat-Nasser and Shokooh [5] initially proposed the pore pressure - dissipated energy relationship. They noted that in a dry granular mass, cyclic loading results in grain rearrangement and volumetric compression causing energy to be dissipated throughout the soil volume. For a saturated soil in undrained conditions, the particles are prohibited from rearranging into a more dense configuration by the pore fluid. Nemat-Nasser and Shokooh postulated that the energy dissipation which resulted in volumetric strain for the dry soil should therefore result in pore pressure increase in the saturated soil. Their idea has since been investigated by a number of researchers [6 – 13]. In several of these publications, comparisons between pore pressure increase and dissipated energy density measured directly in laboratory cyclic loading tests have been displayed. All of the research to date appears to confirm the hypothesis of a well-defined relationship between pore pressure rise and dissipated energy density.

The most simple relationship between pore pressure (p) and dissipated energy (D) is linear

$$p = \alpha D \tag{38}$$

Note that D is the dissipated energy *density* or dissipated energy per unit volume. Therefore D has units of stress and α is a dimensionless constant. Generally values of α in the range 50 to 80 have been suggested by laboratory data. While equation (38) has the benefit of simplicity, it may be inadequate for situations where complete liquefaction is imminent. If p approaches the value of the initial effective stress σ, then one would expect the rate of increase in p to fall off. This has led some investigators to propose a slightly more complex relationship:

$$p = \alpha D^{\beta} \tag{39}$$

This equation permits p to increase more slowly for greater values of D, but suffers from the loss of dimensional homogeneity possessed by equation (38).

In considering the case histories at various sites, we will use equation (38) for most of the calculations, primarily because of its simplicity. In those instances where the linear relationship is clearly inappropriate we will not use (39). Instead we will propose another relationship between p and D. Let

$$\dot{p} = \lambda \dot{D} \tag{40}$$

where

$$\lambda = \lambda(p) = \alpha\left(\frac{\sigma - p}{\sigma}\right) \tag{41}$$

Here the superposed dot implies the time derivative, σ is the initial value of effective stress at the depth of interest, and α is the same as in equation (38). We see from equations (40) and (41) that the pore pressure response for small values of D will be the same as that for equation (38). If the pore pressure increase approaches the value of σ however, the rate of increase will slow and approach zero. Integrating equation (40) gives

$$p = \sigma\left(1 - \exp\left(\frac{-\alpha D}{\sigma}\right)\right) \tag{42}$$

Like equation (39), this model has two parameters; however, one is the initial effective stress, a quantity that presumably can be easily determined. The second parameter α is identical to that in equation (38) and might be expected to lie in the range 50 to 80.

It is a simple matter to integrate the synthesized stress-strain curves discussed in the preceding section to estimate the time history of dissipated energy density D at any depth of interest in the soil profile. Letting τ denote the shear stress and $\dot{\gamma}$ the strain rate, we have

$$D = D(t) = \int_0^t \tau \dot{\gamma}\, dt \tag{43}$$

This calculation can been carried out for any measured earthquake using the synthesized shear stress and strain values for any depth at which a piezometer was located. Both the North-South and the East-West records must be used, the total dissipated energy being their sum. The resulting value for D can then be used with equation (38) or equation (42) to synthesize the pore pressure increase at each piezometer depth for the earthquake. Results from this programme of calculations are shown in the next section.

4

CASE HISTORIES

A total of five earthquakes recorded at four different downhole array sites will be considered. The Kobe Port Island site will be discussed first. Despite the fact no pore pressure measurements were made at Port Island, the occurrence of liquefaction there is well documented.

Kobe Port Island

Port Island was reclaimed by bottom dumping sand and gravel in roughly 15 *m* of water over a period of years beginning in 1966. A bore log from the site of the downhole array is reproduced in Figure 8. In the profile man-made soils lie above 19 *m* while naturally occurring soils are at greater depths. The water table was located at approximately 4 *m* depth. The bore was geophysically logged prior to installation of the downhole array and measured shear wave velocities are also shown on Figure 8. Complete details including SPT data may be found in Iwasaki and Tai [1].

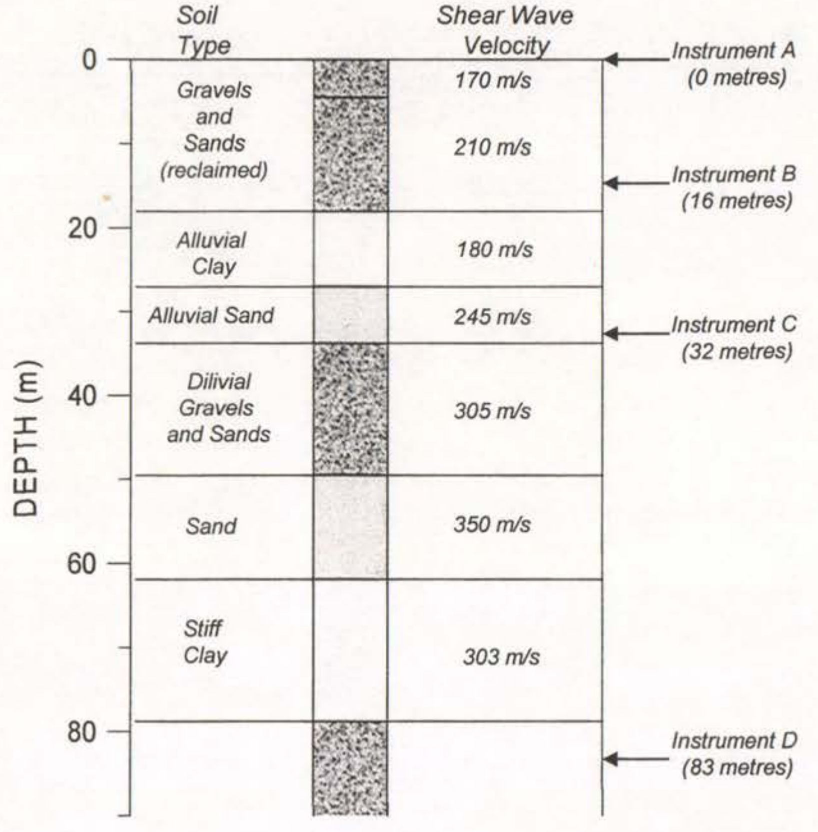

Figure 8. Port Island bore log. Shear wave velocities were obtained from geophysical measurements and represent small strain conditions.

In 1991 four three-component accelerometers connected to a common trigger were installed in the bore at the depths shown on Figure 8. Digitised acceleration records from the downhole array for the Hyogo-ken Nanbu earthquake of 17 January 1995 have been made available by the Committee of Earthquake Observation and Research in the Kansai Area. Figures 2 and 3 show details of the acceleration and integrated displacement time histories for the East-West component of motion. The North-South motions are of a similar intensity.

Details of the synthesised stress – strain response for the Port Island data have been described elsewhere [18, 19, 20]. Here we will consider only the dissipated energy density associated with the stress-strain response. Figure 9 shows graphs of normalised dissipated energy for increments of depth of 1 m throughout the reclaimed layer for all times between 12.5 s and 22.5 s. For each time history in Figure 9, the dissipated energy density D has been normalised by the appropriate value of the initial overburden effective stress σ. We have estimated the effective stress based on a uniform submerged density of 0.80 t/m^3. While this does not adequately account for the soil above the water table, the overall effect on the plotted data is small.

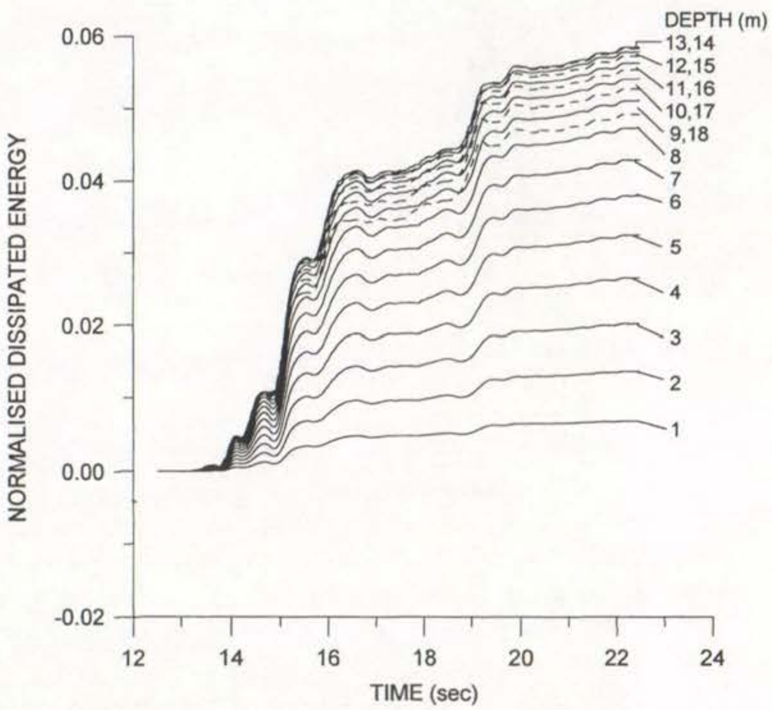

Figure 9. Time histories of dissipated energy density normalised by effective overburden stress. Each curve corresponds to a different depth. Solid lines are used for depths between 1 metre and 13 metres. Dashed lines are used for depths between 14 metres and 18 metres.

Each of the 18 curves plotted in Figure 9 refers to one particular depth and the depth values are indicated on the right hand side of the graph. The highest of the curves corresponds to a depth of 13 m. For greater depths the amount of dissipation decreases, and the curves for 14 through 18 m depths are indicated by dashed lines. It is clear that relatively little dissipation occurs prior to about 14 seconds. At that point the rate of dissipation increases dramatically until about 16 seconds. There is little dissipation between 17 and 19 seconds, but another small jump occurs between 19 and 20 seconds. Only small amounts of additional dissipation occur following 20 seconds.

Using the data in Figure 9, we can construct vertical profiles of normalised dissipated energy density for various times. A selection of profiles is shown in Figure 10. A total of nine profiles are plotted beginning at $t = 14\ s$ and increasing in increments of one second. These profiles seem remarkable for their smoothness but this is in fact a reflection of the smoothness of our interpolating functions. It is again clear from this figure that the bulk of the dissipation happens between 14 and 16 s. The dissipation jump noted on Figure 9 between 19 and 20 s is also evident in this figure.

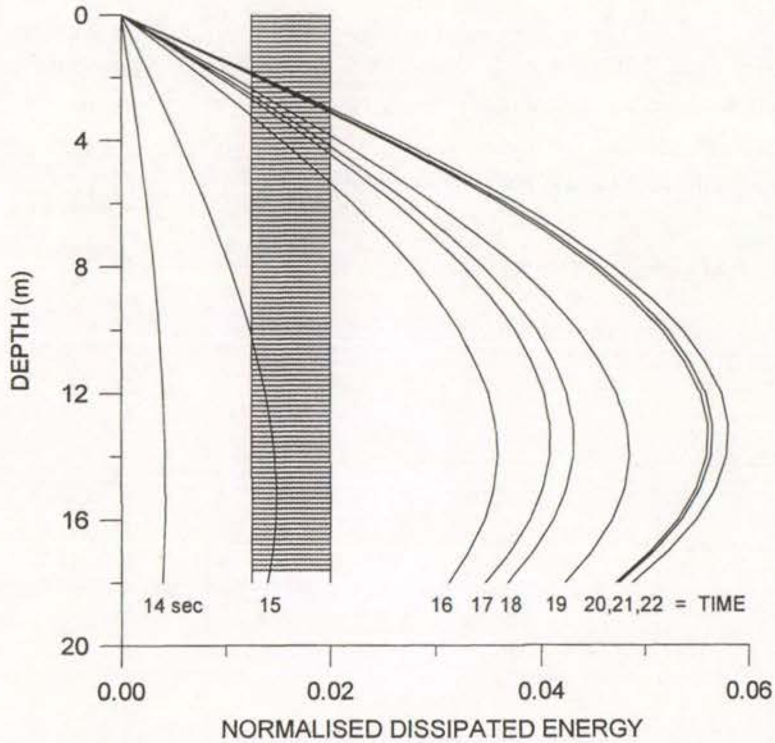

Figure 10. Profiles of normalised dissipated energy density versus depth for various times synthesised from the Kobe Port Island records.

It is interesting to conjecture on the occurrence of liquefaction in the Port Island reclaimed soils. Recalling our discussion in the previous section concerning the relationship between pore pressure increase and dissipated energy, we note that, based on equation (38), the pore pressure u could be expected to approach a value equal to the overburden effective stress σ (indicating complete liquefaction) when the value of the normalised dissipated energy nears $1/\alpha$. The range of values of α suggested by laboratory tests is 50 to 80. Thus we might expect the onset of liquefaction to occur when the normalised dissipated energy enters the range $1/80 = 0.0125$ to $1/50 = 0.02$. This range of values is highlighted on Figure 10. The graph suggests dissipated energy density in the soil crosses the liquefaction threshold at a depth of roughly 15 m and at some time near 15 s. A zone of liquefaction would then grow with time in both upward and downward directions. We can easily follow the progress of this zone as shown in Figure 11. The two lines trace the development of the liquefied zone for either of the two α values. Referring to the $\alpha = 80$ case, we see the zone of liquefaction quickly moves downward to the base of the gravel layer. It also moves upward to a depth of roughly 4 *m* and then increases much more slowly. In reality the water table is near 4 *m* and liquefaction would be impossible above that point. The line corresponding to $\alpha = 50$ has a similar shape to that for the larger α value but the onset of liquefaction occurs slightly later and the propagation of the zone is slightly slower. Note that our analysis here is based on equation (38) rather than equation (42) despite the fact complete liquefaction occurred. This is due to the nature of equation (42) where u can approach σ asymptotically but never actually reach the value of σ.

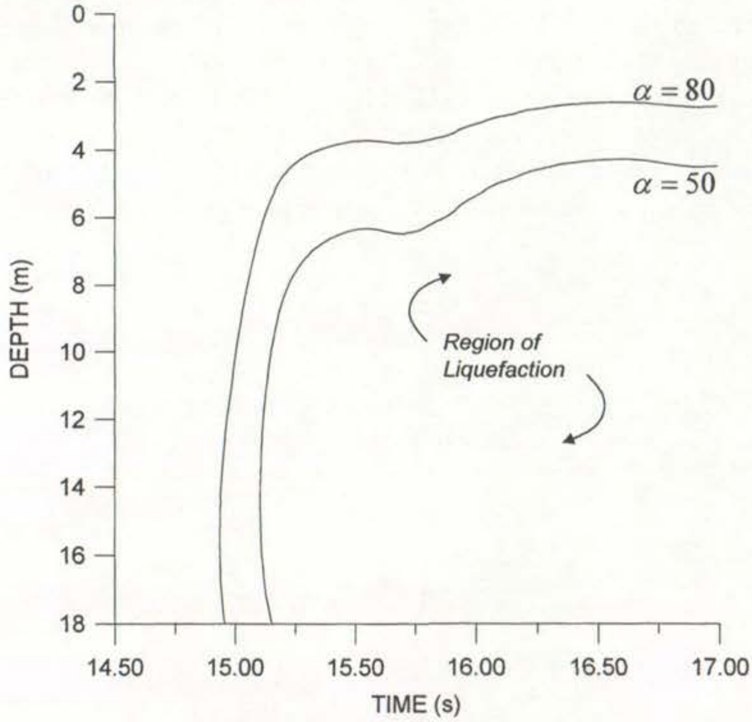

Figure 11. Growth of the zone of liquefied soil at Port Island synthesised from downhole recordings.

It is unfortunate the Port Island array was not instrumented with pore pressure transducers and hence we have no measurements with which to compare. Nevertheless, there was ample surface evidence to ensure liquefaction did occur. Also, other investigators [19] have suggested liquefaction developed within exactly the same time frame as suggested here. While this cannot be construed as a validation for the *D-p* hypothesis, it does point in the right direction.

Lotung

The SMART1 downhole array at Lotung has been described by several investigators [2, 21, 22, 23]. Records from Lotung have been used by Zeghal, *et al.* [16] to approximate shear stress and strain using a method similar to ours, however they did not consider dissipated energy and pore pressure increase as we do here. The earthquake we consider occurred on 14 November 1986. It is referred to as Event 16 in the SMART1 catalogue. Its local magnitude was 7.0 and epicentral distance 78 *km*.

Soils at the Lotung site consist of interbedded silty sands and sandy silts to a depth of about 30 *m*. The water table is found within approximately 1 *m* of the ground surface. The site stratigraphy is considered to be sufficiently uniform to permit a single layer model for the stress and strain calculations.

The SMART1 array consisted of 15 three-component accelerometers placed on the ground surface and two downhole accelerometer sets denoted DHA and DHB. A visual comparison of the acceleration records from the DHB array is shown in Figures 12(a) and (b). Peak acceleration was approximately 170 cm/s^2 found at the ground surface in the North – South component. The records shown in Figure 12 have been treated with a band pass filter. Zeghal, *et al*. [1995], in relation to the same data, suggested a filter with cut-off frequencies of 0.35 *Hz* and 6.0 *Hz*. For our calculations we have chosen a lower cut-off of 0.1 *Hz* combined with an upper ramp cut-off decreasing linearly between 6.0 *Hz* and 7.0 *Hz*. The difference between our filter and that used by Zeghal *et al*. is small with regard to calculation of dissipated energy.

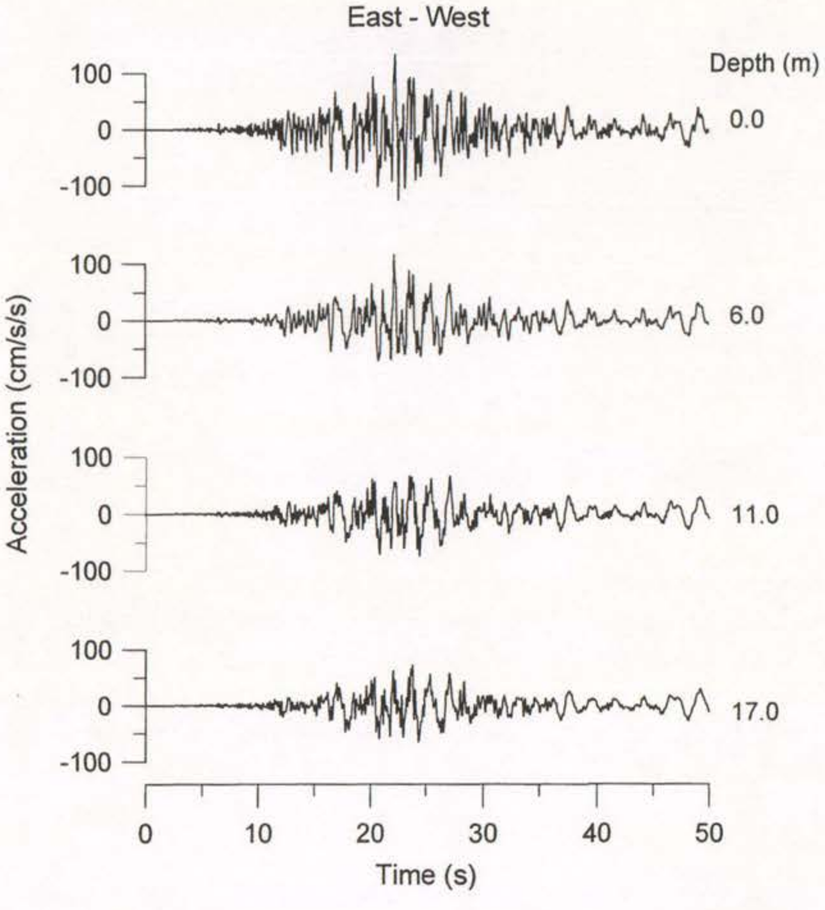

Figure 12a. Measured accelerations from Lotung. East-West component.

Figure 13 gives the main result of our study of the Lotung records. The five pore pressure time histories measured at the site are plotted (dashed lines) together with corresponding calculated values of p based on dissipated energy density using equation (38). Note the pore pressure transducer designations shown on the right hand side of the figure. The depths corresponding to each instrument are shown in Table 1. Each of the calculated pore pressure histories was determined for the depth corresponding to the depth of measurement. In all five cases the value of the parameter α was set equal to 50.

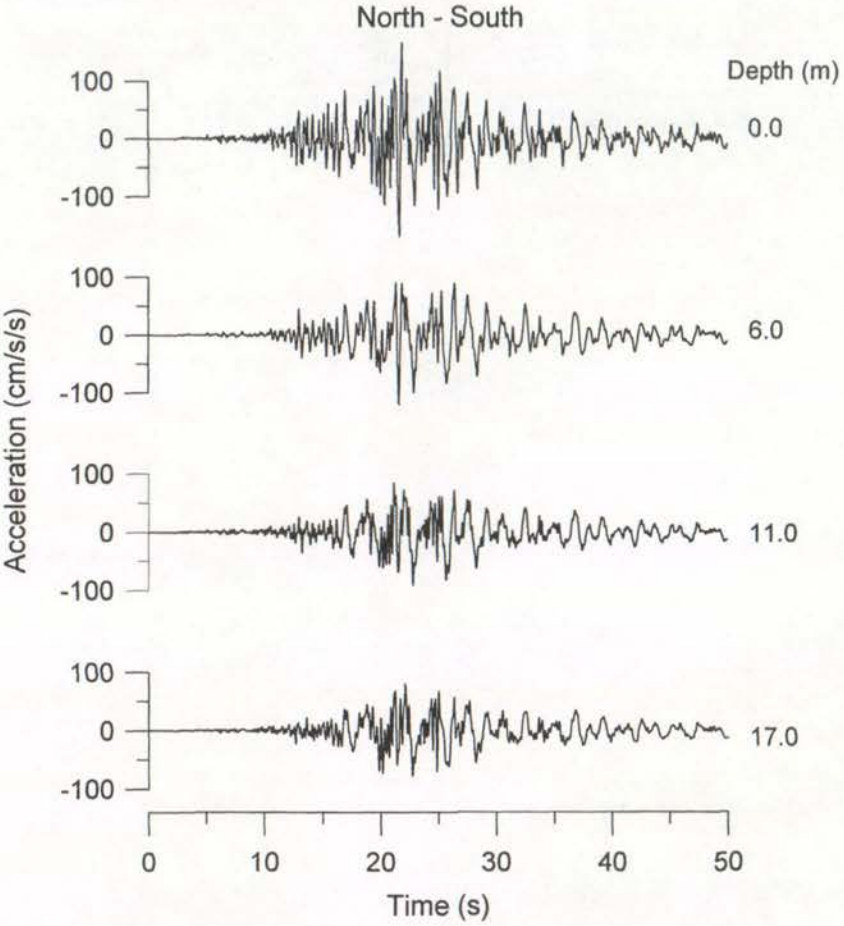

Figure 12b. Measured accelerations from Lotung. North-South component.

TABLE 1. Pore Pressure Measurement Depths - Lotung

Instrument designation	*Depth*
PF-8	15.0 m
PN2-1	6.3 m
PA-3′	5.1 m
PN2-2′	8.0 m
PN3-1	6.38 m

In Figure 13 it is clear the instrument PF-8 record is contaminated by significant amounts of noise. No explanation for this is available. The remaining instrumental records show varying degrees of noise with PN3-1 showing the least. Careful inspection of the measured records reveals that after about 30 seconds all five measured pore pressures begin to slowly decrease. This is no doubt due to natural dissipation of pore pressure caused by flow of the pore fluid.

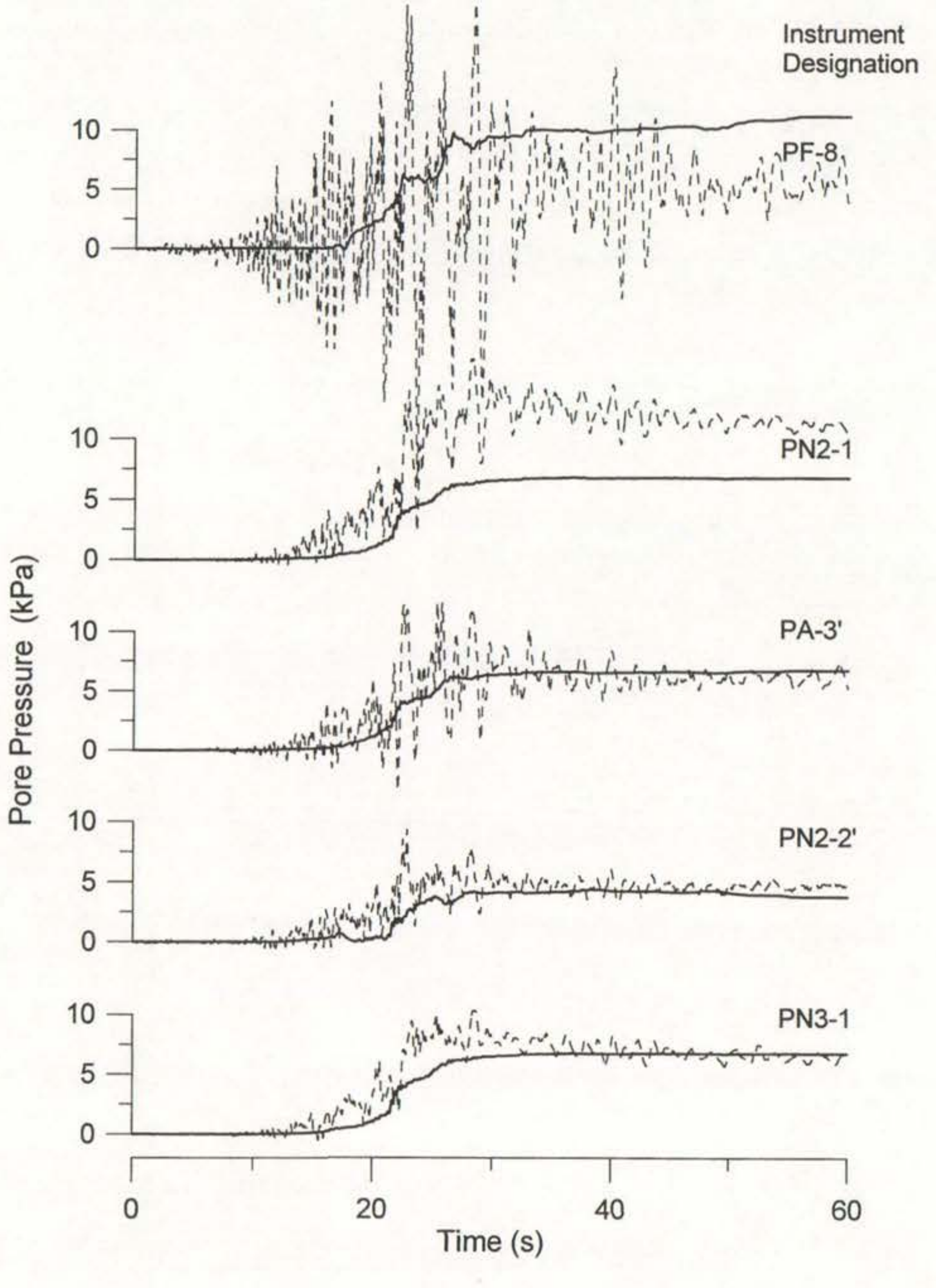

Figure 13. Measured and calculated pore pressure increase for Event 16, Lotung.

For three of the records, PA-3′, PN2-2′ and PN3-1, the correlation between measured and calculated values is remarkably close. Of the remaining two records, the calculated value for PF-8 is high while that for PN2-1 is low. In all cases the onset of pore pressure increase is remarkably well modeled by the calculated data. Figures 14 and 15 show expanded views of the PA-3′ and PN3-1 records for times between 15 and 30 seconds. In the figures two calculated pore pressure histories are shown. Both are based on equation (38), one for $\alpha = 50$ and the other for $\alpha = 80$. These values are the limits on α suggested by laboratory test data. One would naturally expect different soils to be characterised by different values of α. The Lotung data appear to indicate the range of laboratory α values, 50 to 80, is be sufficient to encompass the behaviour of the test site soils. The more complex *D-p* relationship (42) is not required here since the greatest excess pore pressure generated is roughly only ten percent of the overburden effective stress.

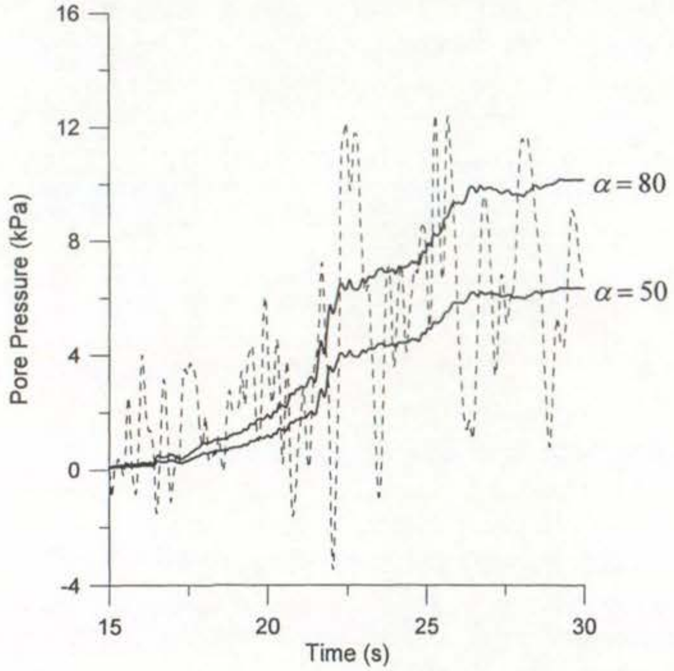

Figure 14. Expanded view of PA-3′ record from Lotung.

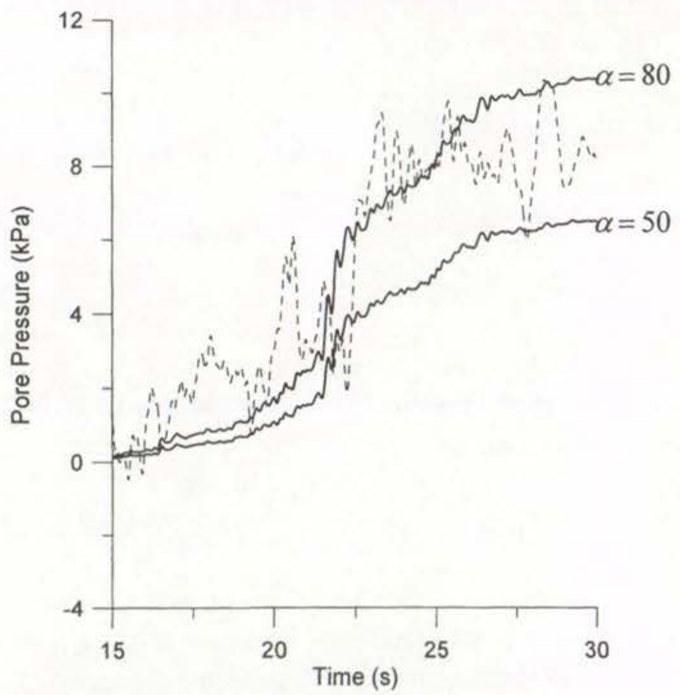

Figure 15. Expanded view of PN3-1 record from Lotung.

Sunamachi

The Sunamachi test site was established near Tokyo in 1986 [3]. Four downhole accelerometers at depths between 1.07 *m* and 89.5 *m* were installed together with four pore pressure transducers at depths between 7 *m* and 12.9 *m*. Table 2 shows the designations and depths for each of the pore pressure transducers. Transducers W3 and W4 were located approximately 60 *m* horizontally distant from the accelerometer array and the other two pore pressure transducers.

TABLE 2. Pore Pressure Measurement Depths - Sunamachi

Instrument Designation	*Depth*
W1	10.0 m
W2	7.4 m
W3	12.9 m
W4	7.0 m

The soil profile at the site is complex, having been subjected to significant man made alterations over a period of years. The water table ranges in depth from 3 to 6 *m*. Details of the site soils are given by Ishihara, *et al.* [3]. For purposes of our stress and strain calculations we have used a simplified profile summarised in Table 3. Note that the values of elastic shear wave velocity are not essential information for the stress-strain computation, although the ratio of velocities is required. This point is discussed in Davis and Berrill [15].

TABLE 3. Sunamachi Soil Profile Parameters

Layer Number	*Soil Type*	*Thickness*	*Elastic Shear Wave Velocity*
1	Sands and Silts	13.7 m	220 m/s
2	Silty Clay	36.5 m	130 m/s
3	Sandy Gravel	∞	550 m/s

The earthquake we will consider occurred 17 December 1987. It is known as the Chiba-Toho-Oki earthquake with magnitude 6.7 and epicentral distance approximately 60 *km*. Figures 16(a) and (b) show the measured accelerations from the downhole array. Maximum acceleration of roughly $120\,cm/s^2$ occurred at the ground surface in the East-West component. We have filtered the acceleration records using the same filter parameters as noted above for the Lotung data.

Figure 17 shows plots of measured dynamic pore pressure increase compared with calculated pore pressure histories found from the *D-p* model. The value of α for all calculated data is 80. Clearly agreement here is not quite so good as for the Lotung records, but must nevertheless be regarded as excellent. Perhaps the most striking feature to be seen on Figure 17 is the similarity of the measured and calculated values during the period of rapid pore pressure rise between 20 and 24 seconds. After 24 seconds, dissipation of measured pore pressure due to flow becomes quite pronounced and the measured and calculated values begin to diverge. Evidently

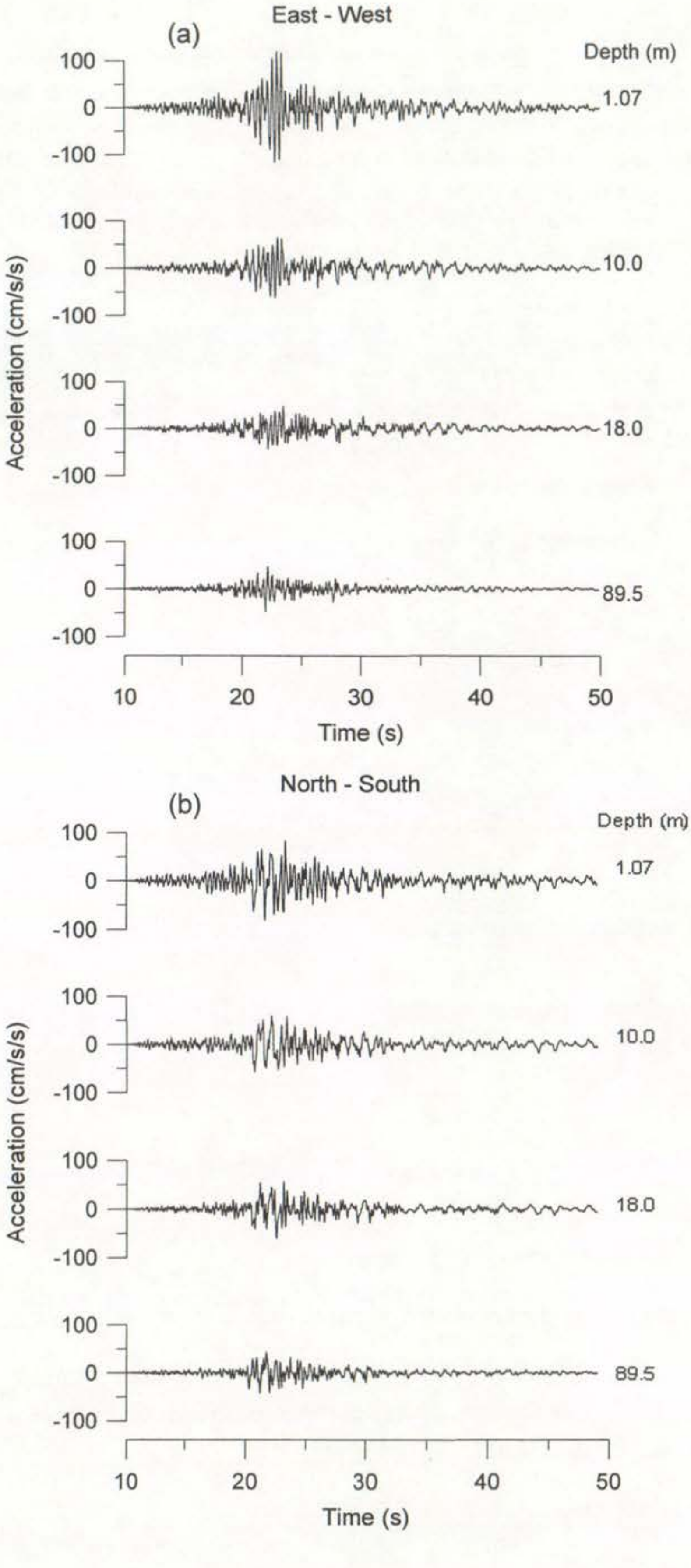

Figure 16. Measured accelerations from Sunamachi.

the Sunamachi soils are generally more free draining than those at Lotung. The dissipated energy continues to increase slowly following the rapid rise between 20 and 24 seconds. Poorest agreement for the Sunamachi data is found for pore pressure transducer W2. The measured record is obtained at nearly the same depth as W4 where excellent agreement is found. We can offer no explanation for the W2 data other than the possibility that local conditions may have offered enhanced drainage around this transducer.

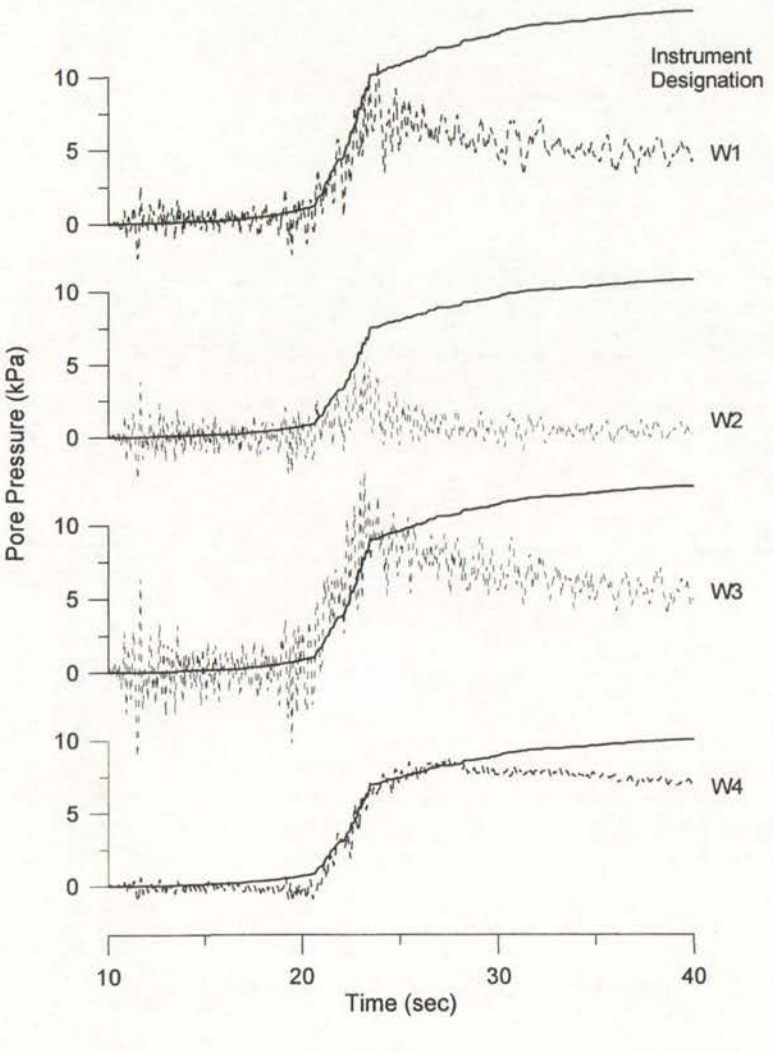

Figure 17. Measured and calculated pore pressure increase from Sunamachi.

In Figure 18 we show at an expanded scale that part of the W1 record for which pore pressure is rapidly rising. As in Figures 14 and 15, we have plotted calculated pore pressures for both values of α: 50 and 80. Evidently this range is sufficient to adequately model the Sunamachi test site soils as well.

Like the Lotung data, the excess pore pressures at Sunamachi were roughly ten percent of effective overburden stress, and therefore the soils were well clear of complete liquefaction. Despite this, the two sets of data provide considerable encouragement for the *D-p* hypothesis. Perhaps the most remarkable aspect of the results for both Lotung and Sunamachi is the near absence of parameters that can be adjusted in order to fit the calculated values to the measured values of pore pressure. The only things we can adjust are first, α, second, the filter cutoff values, and third, in the Sunamachi case, the depths and ratios of shear wave velocities for the soil layers. We have used values of α that are representative of laboratory test data. Our filter parameters are similar to those used by Zeghal, *et al.* [16] in relation to the Lotung data. The layered model for Sunamachi was determined simply by inspecting the bore logs published by Ishihara *et al.* [3]. Our point is this: the agreement found above is not the result of adjusting values of model parameters. Instead, we are in effect presenting data directly from a full scale experiment in which dissipated energy density multiplied by a single dimensionless number α falls remarkably close to measured pore pressure increase.

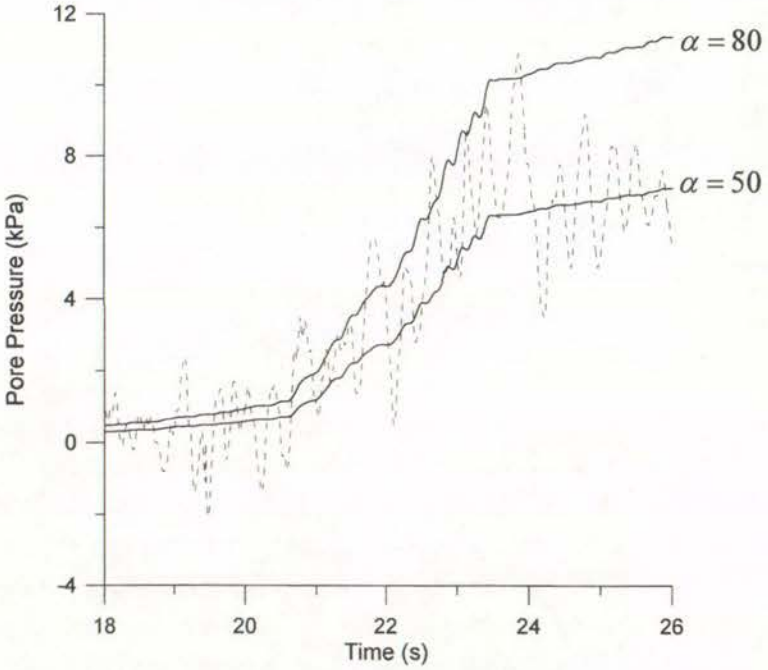

Figure 18. Expanded view of W1 record from Sunamachi.

Wildlife

In November 1987, two earthquakes occurred near a site in the Imperial Valley, California, where extensive field instrumentation had been placed by the US Geological Survey. The site was part of a wildlife refuge and has come to be called the Wildlife Site, or simply Wildlife. The Wildlife Site became of interest following the Westmorland earthquake in 1981. That earthquake appeared to have caused liquefaction in certain areas, Wildlife being one. The site was subsequently instrumented with two accelerometers, one at $-7.5\,m$ depth below ground surface and one at ground surface; and with six piezometers at depths ranging between $-2.9\,m$ and $-12.0\,m$. Site stratigraphy is illustrated in Figure 19. A layer of silt approximately $2.5\,m$ thick overlies a $4.5\,m$ thick layer of silty sand. The silty sand was presumed to be the liquefiable soil at the site. It lay above a $5\,m$ thick layer of stiff clay. Of the six piezometers, five were placed in the silty sand layer. The ground water table was located at a depth of approximately $1.2\,m$. The downhole accelerometer was positioned near the upper surface of the stiff clay.

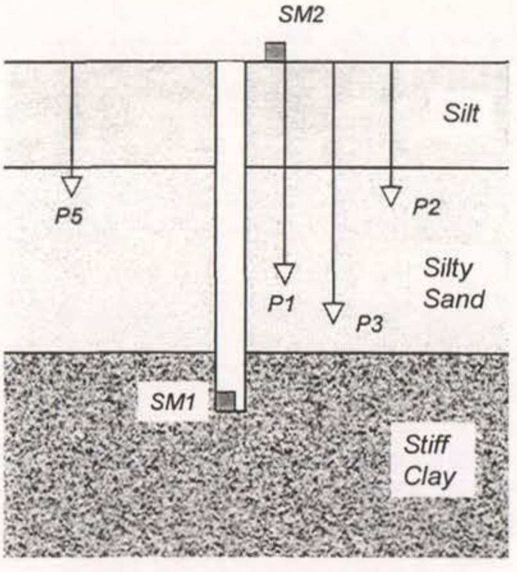

Figure 19. Soil profile at Wildlife.

In November 1987, two earthquakes occurred near Wildlife within a period of 12 hours. The first was the Elmore Ranch earthquake. It had magnitude 6.2 and was located approximately $23\,km$ west from Wildlife. The second was the Superstition Hills earthquake, magnitude 6.6, located approximately $31\,km$ to the west and south from Wildlife. At the ground surface the peak measured acceleration for the Elmore Ranch event was $0.13\,g$, and for the Superstition Hills event, $0.21\,g$. None of the field piezometers indicated significant pore pressure increase for the Elmore Ranch event, but four piezometers located in the silty sand layer recorded large pore pressure changes for the Superstition Hills event. One other piezometer in the silty sand did not operate properly and the sixth piezometer was located in deeper soil below the liquefying layer.

Holtzer, et al. [4], reported on the measured pore pressures from the Superstition Hills event. They suggested the silty sand layer had liquefied during the earthquake. Their suggestion was based on both the recorded pore pressures and on surface evidence of sand boils and lateral spreading features. Subsequently questions were raised concerning the unexpectedly long rise times recorded by the pore pressure transducers. When compared with the duration of strong ground shaking, it appeared to some analysts that the measured pore pressure response was considerably slower than seemed reasonable. Because of this, Hushmand, *et al.* [24] attempted to recalibrate the field piezometers *in situ*. They tested each of the existing piezometers by inserting a new piezometer close by and then artificially generating a pore pressure pulse in the ground. They then compared the readings of the existing and newly inserted piezometers. The comparisons revealed that the response of the existing piezometers was similar to that for the newly inserted instrument in only one case. Hushmand, *et al.* [24] did not suggest liquefaction might not have occurred. Indeed everyone seems to agree liquefaction did occur. They did suggest, however, that the pore pressure response rise times might be too slow.

Subsequent to the recalibration experiments by Hushmand, *et al.* [24], Youd and Holtzer [25] defended the original pore pressure recordings. They noted how interbedding of silt and sand at the site might possibly affect the response of two piezometers separated by small but significant distances. They also noted how the ground motion at the site continued for many seconds beyond the period of strong shaking and how this motion may have contributed to pore pressure generation. For further corroboration they cited the analysis by Zeghal and Elgamal [26] in which the measured accelerations were used to estimate the shear stress-strain time history within the upper most $7.5\,m$ of soil. Zeghal and Elgamal's analysis showed that softening of the site soils continued to occur beyond the period of strong shaking.

The Wildlife records remain a unique resource in the field of earthquake geotechnical engineering. While the fidelity of the pore pressure recordings can never be guaranteed with complete confidence, the arguments from both sides of the issue are persuasive. One thing is certain, the Elmore Ranch earthquake caused no pore pressure increase, but the Superstition Hills earthquake caused complete liquefaction. The major difference between the two events was a very brief period of stronger shaking in the Superstition Hills earthquake. That brief period may have acted as a trigger, setting the pore pressure rise mechanism in motion. Subsequent lesser ground shaking, similar to the Elmore Ranch earthquake, then continued to induce greater pore pressure until liquefaction resulted. The idea of a trigger or critical value of shaking is quite similar to the threshold shear strain theory of Dobry *et al.* [27]. They suggested a critical strain value exists for which large scale grain rearrangement will commence. For smaller strain levels, the intergranular contacts would remain elastic or elastic-plastic, but complete slip would not occur. At the threshold strain, the entire contact slips and the grains begin to displace relative to one another. Only minor pore pressure changes can occur prior to the threshold strain. Once the threshold is reached, large pore pressure increases may occur.

Figure 20 shows the measured acceleration time histories for the Elmore Ranch earthquake. Figure 21 shows the comparable data for the Superstition Hills event. Note that the vertical acceleration scale in both figures is the same but the time scales are different. Note also how the Superstition Hills surface records display peculiar acceleration spikes separated by more or less flat response at later times. This pattern is thought to be indicative of liquefied soil behaviour [28]. Comparing the two sets of records, it is clear the Superstition Hills event was stronger, but the differences are not great.

If we carry out the synthesis of stress and strain and calculate the dissipated energy density for the Elmore Ranch records, we find only very small amounts of predicted pore pressure increase. Even with the value of α set equal to 200, the maximum predicted excess pore pressure for Elmore Ranch turns out to be only 1.3 *kPa*. The very small measured pore pressures for this event corroborate this result. The measured pore pressures for Elmore Ranch were so small the researchers involved did not bother to digitize the records [29].

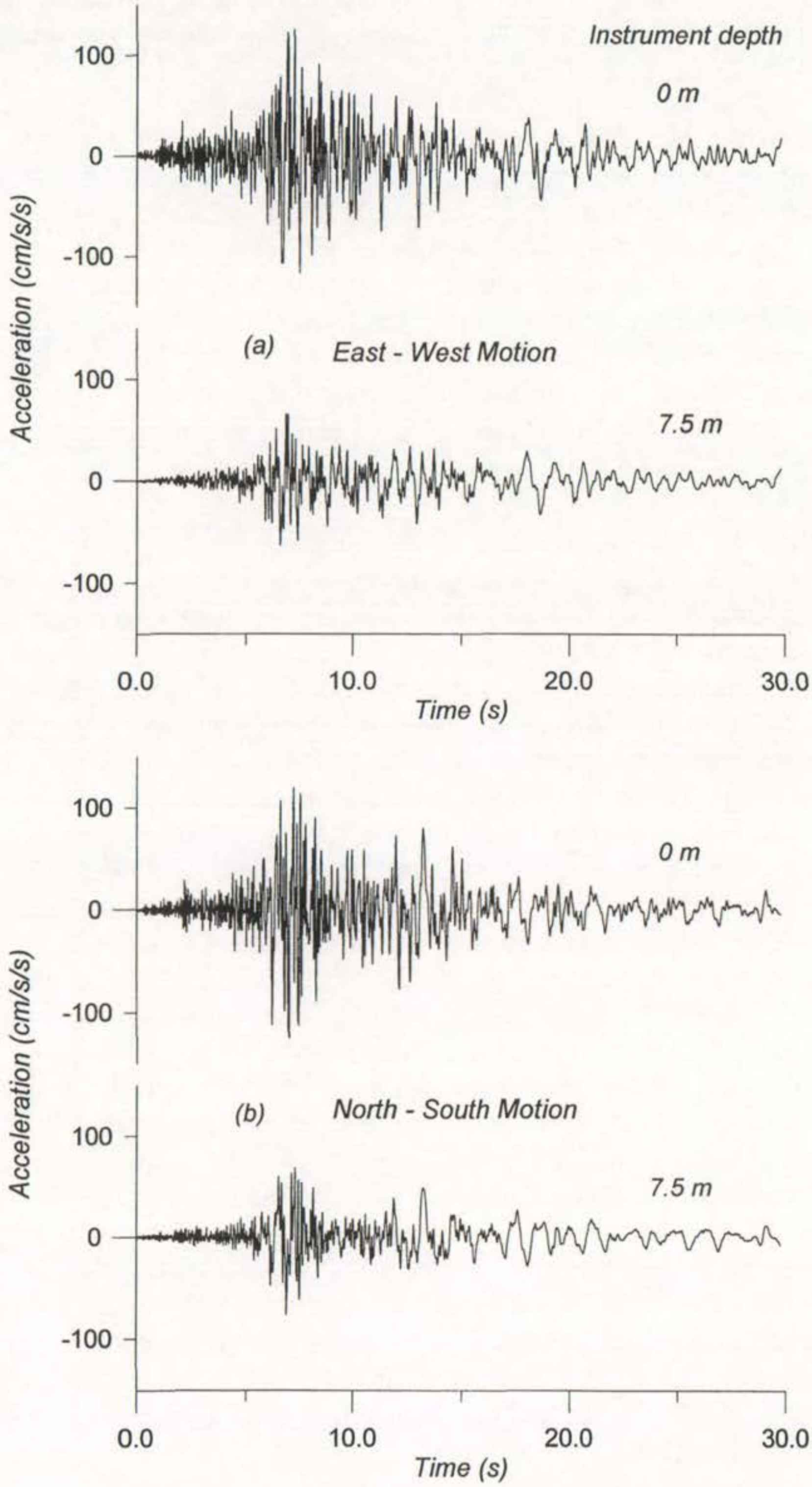

Figure 20. Measured accelerations for Elmore Ranch earthquake

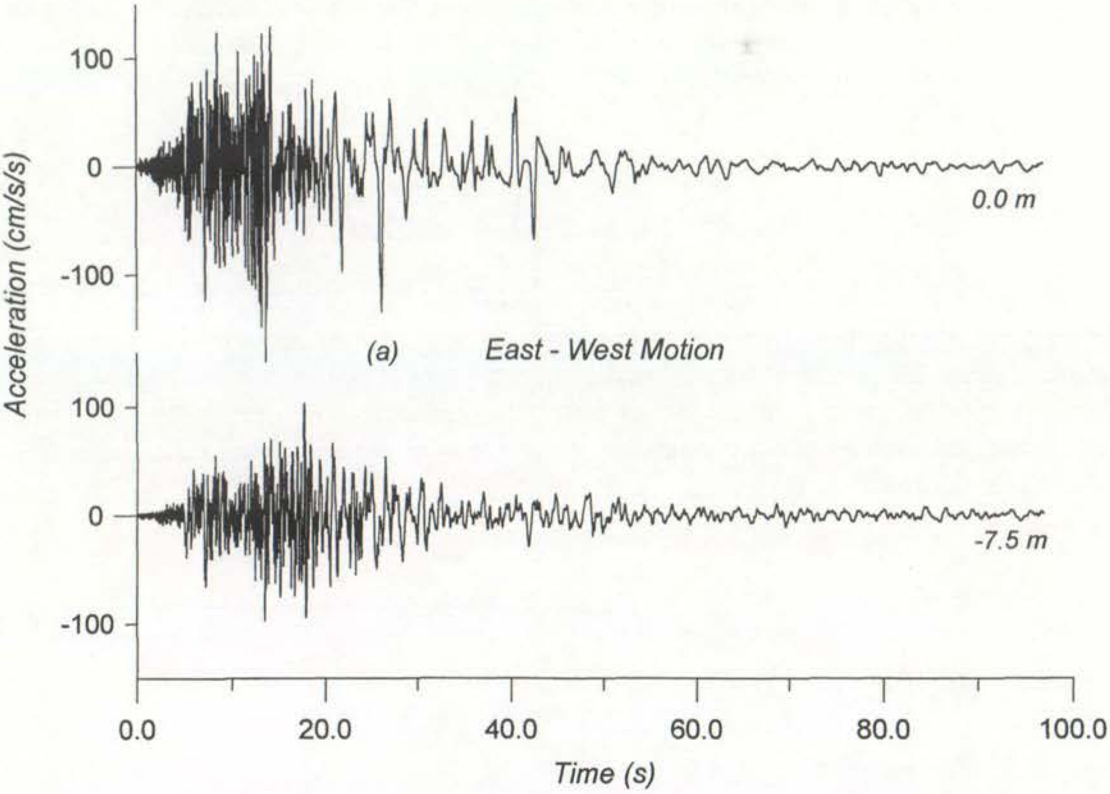

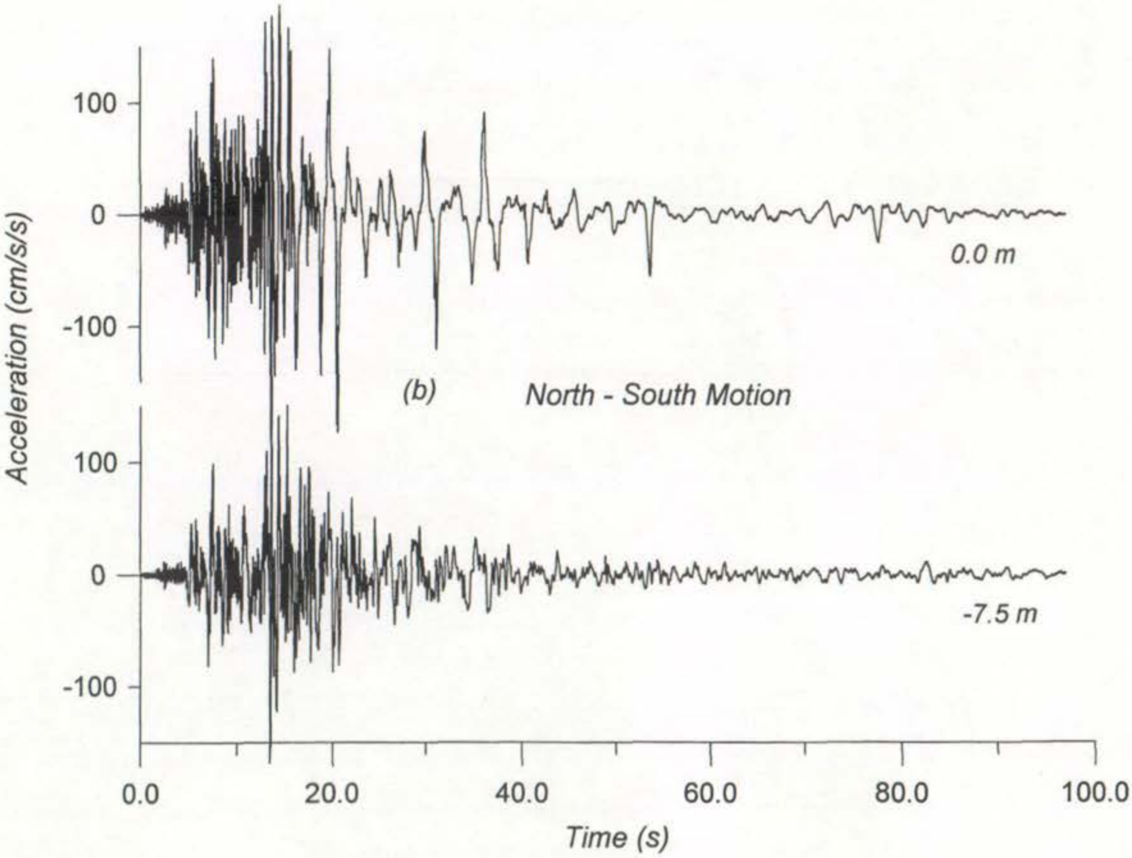

Figure 21. Measured accelerations for Superstition Hills earthquake

TABLE 4. Pore Pressure Measurement Depths – Wildlife

Instrument Designation	*Depth*
P1	5.0 m
P2	3.0 m
P3	6.6 m
P5	2.9 m

In contrast, the predicted pore pressures for the Superstition Hills event are quite large. Figure 22 shows the calculated pore pressures together with the measured data for the four field piezometers of interest. (Piezometer *P4* failed to function during the earthquake, while piezometer *P6* was placed in the stiff clay and is of no interest for liquefaction.)

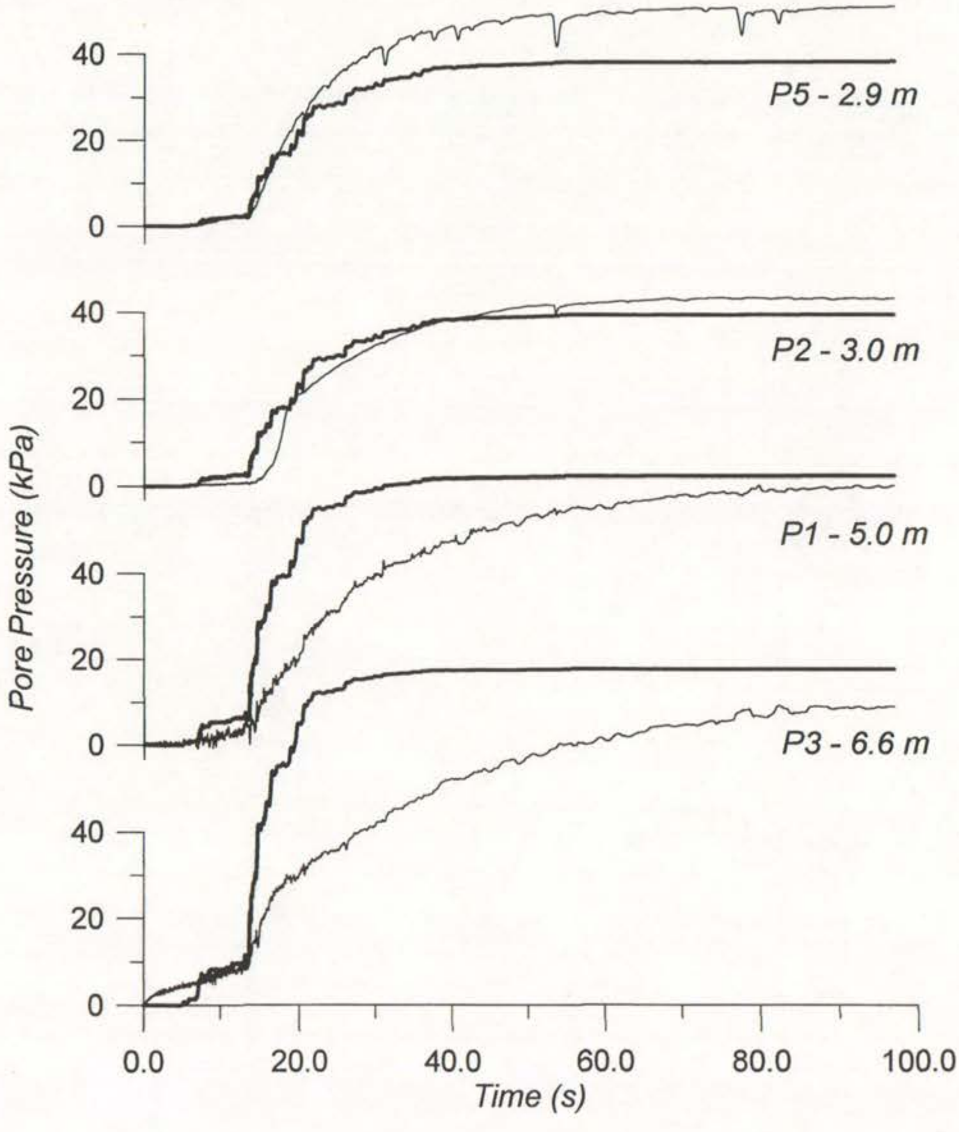

Figure 22. Measured and predicted pore pressures for Superstition Hills earthquake.

In Figure 22 the lighter lines represent measured data and the heavier lines represent our predictions. Depths for the four piezometers are shown on the Figure as well as in Table 4. The pore pressure predictions shown were generated using equation (42) since complete liquefaction evidently did occur. Values for the overburden effective stress were inferred from data given in [25]. The value of α used in this simulation was 200, significantly greater than the α values used for Lotung and Sunamachi, as well as for laboratory results. The significance of such a large α value is discussed below.

It is immediately evident from Figure 22 that the *P2* and *P5* records are fairly well represented by the calculated pore pressure response. The measured data for *P5* are slightly anomalous to begin with since the peak measured pore pressure rise exceeded the initial effective stress σ by roughly 20 percent (Youd and Holtzer, [25]). Clearly, the format of equation (42) will not permit the calculated value of p to exceed the initial effective stress. Thus we cannot expect better agreement for *P5* than that shown. The response of *P2*, at nearly the same depth, lies closer to the expected value of the initial effective stress. At greater depths the modeled pore pressure increase occurs more quickly. This results from greater dissipation of energy deeper in the layer caused by greater stresses and strains. This comment can be generalised. The free surface boundary condition ensures no dissipated energy can occur at zero depth. In general then, for a homogeneous material, dissipated energy density must increase with increasing depth. In a layered soil profile the generalisation may break down; but, as a rule of thumb, the pore pressure should increase more quickly as one moves deeper in the soil profile. It does not necessarily follow that liquefaction will occur sooner since the effective overburden stress is greater The measured response for *P1* and *P3* both show much slower pore pressure increases than is seen at the higher locations of *P2* and *P5*. Both *P1* and *P3* measurements appear to be converging on the calculated p values, but the rate of pore pressure rise appears quite slow. Criticism of the field piezometer measurements by Hushmand, *et al.* [24] focused on the slow response recorded by these two instruments. Hushmand, *et al.* found that only piezometer *P5* responded accurately in their calibration tests. Partial saturation of the piezometers when initially placed at the site was suggested in [24] as a possible mechanism leading to slow response. It seems, therefore, that we may have some confidence in assuming the measured pore pressures for piezometers *P1* and *P3* are not totally accurate.

As noted above, the value of α used to generate the theoretical curves in Figure 22 is considerably greater than might be expected following from results for Lotung or Sunamachi, or for laboratory tests. Smaller values of α can be used but the agreement with the experimental data breaks down fairly rapidly if α is decreased. The high value for α suggested here may be due to the nature of the Wildlife soil. Whereas most laboratory data have been generated using clean sands, the soil at Wildlife is described by Youd and Holtzer [26] as a thinly cross-bedded silty sand. The fines content $(< 0.075\,mm)$ is given by Holtzer *et al.* [24] as about 33 percent. In the usual context of liquefaction studies, the large silt content at Wildlife is atypical. It may be that the large fines content requires a larger value for α. An alternative explanation is simply that the dissipated energy density is not a valid indicator of pore pressure increase in soils of this type. While this may be true, the agreement between measured and computed pore pressures at the *P2* and *P5* depths suggests otherwise. A definitive answer to the question of the magnitude of α will await the collection of more data from both field and laboratory.

5

CONCLUSIONS

The results presented in this report seem to strongly point toward validation of the *D-p* hypothesis. In judging this conclusion one must consider several aspects of the problems involved in field instrumentation and interpretation of field data. First it is important to keep sight of the central role played by the measured acceleration data. Without field accelerations there could be no synthesis of stress and strain and hence no calculation of dissipated energy density. The computational aspects of synthesising strain and stress are straightforward and, especially in cases where downhole instruments are spaced relatively closely, we can have considerable confidence in the results. Once stresses and strains are known, calculation of dissipated energy density is a trivial matter. The second part of the overall picture is the role of the field piezometer data. Dynamic pore pressure measurement is not a simple matter and pore pressure results need to be considered with care. Indeed, dynamic pore pressures can be difficult to measure in the laboratory much less several metres below ground in a strong earthquake. The effects of electronic noise may constitute a problem for data interpretation and careful piezometer saturation prior to placement is clearly important.

The third and most crucial aspect of our result is the role of the pore pressure – dissipated energy relationship. There is no fundamental reason for believing such a relationship exists. The *D-p* hypothesis [5] was originally based on a loose theoretical development relying heavily on a comparison of response of dry sand with similar saturated sand. Where loose dry sand might be expected to contract during short term shaking, saturated sand cannot because of the necessity for flow. Energy dissipation must occur in the dry sand since volumetric strains accompany the shaking and there will inevitably be stresses involved. The integral of stress multiplied by strain rate automatically gives dissipated energy density. No similar calculation is possible for the saturated sand since no volumetric strain occurs. Distorsional strains do occur and they are accompanied by dissipation in the solid particle skeleton, but how this effect is coupled to the pore fluid is not clear. Nemat-Nasser and Shokooh [5] considered these aspects and hypothesised that energy lost in volumetric straining of the dry material is converted to pore pressure in the saturated material.

The absence of fundamental justification for *D-p* relationship does not impede its application. Like many other relationships that describe aspects of material behaviour, we can turn to experimental evidence to justify its use. This is easier to do in the laboratory, and has been accomplished by several investigators [8, 9, 10]. In this we report we have simply attempted to carry on the process with field data. The main results of our work are embodied in Figures 13, 17 and 22. In the case of Lotung and Sunamachi, relatively small pore pressure rises were measured and these were well represented by the *D-p* model. At Wildlife complete liquefaction occurred but validity of the data is, to some extent, open to question. Nevertheless, the *D-p* hypothesis works reasonably well for this case too. Our results present a strong argument in favour of dissipated energy to be placed alongside the existing laboratory data.

One may raise an interesting question at this point concerning the roles of cause and effect. It might be argued that increased dissipation is the result of increasing pore pressure, rather than the other way around. It is certainly true that increased pore pressure will result in softening and hence greater strains in any soil, and greater strains will presumably be accompanied by more dissipated energy. This argument would explain the simultaneous onset of dissipation and pore pressure displayed so well in all our field results. It will not, however, satisfy the later stages of observed response. If pore pressure leads to dissipation rather than the reverse, one would expect to see continued growth of dissipated energy in the Lotung and Sunamachi data after pore pressure growth has ceased. This is observed to some extent at Sunamachi, but clearly is not seen in the Lotung data. At Wildlife the effect is not so clear since complete liquefaction occurred and little dissipation can occur under those conditions since the propagation of shear stress is greatly impeded. Increasing pore pressure will always imply decreasing effective stress and hence a decrease in the ability of the solid particle matrix to dissipate energy frictionally. The interplay between increasing strains and decreasing effective stress is complex and no precise answers may be given, but the Lotung data clearly support the *D-p* hypothesis.

It will be extremely interesting to await the occurrence of more earthquakes near instrumented sites. The data we possess to date is limited both by small number of events and by the fact that only one event involved complete liquefaction. A large number of downhole arrays have been installed in both Southern California and Japan. Like so many aspects of earthquake engineering, the *D-p* hypothesis must now await the next earthquake before further development is possible.

REFERENCES

1. Iwasaki, Y., and M. Tai, 'Strong motion records at Kobe Port Island', *Soils and Foundations, Kobe Earthquake Special Issue*, pp. 29-40 (1996).

2. Wen, K.-L., Beresnev, I.A. and Yeh, Y.T., 'Investigation of non-linear site amplification at two downhole strong ground motion arrays in Taiwan, *Earthq. Engrg. Struct. Dyns.*, **24**, 313-324 (1995).

3. Ishihara, K., Muroi, T., and Towhata, I., 'In-situ pore water pressures and ground motions during the 1987 Chiba-Toho_Oki earthquake', *Soils and Foundations*, **29**, No. 4, 75-90 (1989).

4. Holzer, T.L., T.L. Youd and T.C. Hanks, 'Dynamics of liquefaction during the 1987 Superstition Hills, California, earthquake', *Science*, **244**, pp. 56-59 (1989).

5. Nemat-Nasser, S., and Shokooh, A.,'A unified approach to densification and liquefaction of cohesionless sand in cyclic shearing', *Canadian Geotech. Jour.*, **16**, 659-678 (1979).

6. Davis, R.O., and Berrill, J.B., 'Energy dissipation and seismic liquefaction in sands', *Earthq. Engg. Struct. Dyns.*, **10**, 59-68 (1982).

7. Berrill, J.B., and Davis, R.O., 'Energy dissipation and seismic liquefaction in sands: Revised model', *Soils and Foundations*, **25**, no. 2, 106-118 (1985).

8. Simcock, K.J., Davis, R.O., Berrill, J.B., and Mullenger, G., 'Cyclic triaxial tests with continuous measurement of dissipated energy', *Geotech. Testing Jour.*, **6**, 35-39 (1983).

9. Law, K.T., Cao, Y.L., and He, G.N., 'An energy approach for assessing seismic liquefaction potential', *Canadian Geotech. Jour.*, **27**, 320-329 (1990).

10. Figueroa, J.L., Saada, A.S., Liang, L., and Dahisaria, M.N., 'Evaluation of soil liquefaction by energy principles', *Jour. Geotech. Engg. Div.*, ASCE, **120**, 1554-1569 (1994).

11. Liang, L., Figueroa, J.L., and Saada, A.S., 'Liquefaction under random loading: Unit energy approach', *Jour. Geotech. Eng. Div.*, ASCE, **121**, 776-781 (1995).

12. Trifunac, M., 'Empirical criteria for liquefaction in sands via standard penetration tests and seismic wave energy', *Soil Dyns. Earthq. Engg.*, **14**, 419-426 (1995).

13. Kayen, R.E. and Mitchell, J.K., 'Assessment of liquefaction potential during earthquakes by Arias intensity', *Jour. Geotech. & Geoenv. Engg.*, ASCE, **123**, 1162-1174 (1997)

14. Davis, R.O. and Berrill, J.B., 'Site specific prediction of liquefaction', *Geotechnique*, **48**, 289-293 (1998).

15. Davis, R.O. and J.B. Berrill "Rational approximation of stress and strain based on downhole acceleration measurements", *Int. J. Numer. Anal. Meth. Geomech.*, **22**, 603-619 (1998).

16. Zeghal, M., Elgamal, A-W., Tang, H.T. and Stepp, J.C., 'Lotung Downhole Array. II: Evaluation of Soil Nonlinear Properties', *Jour Geotech. Engg.*, ASCE., **121**, 363-378 (1994).

17. Haskell, N.A., 'Crustal reflection of plane SH waves', *Jour. Geophys. Res.*, **65**, 4147-4150 (1960).

18. Davis, R.O. and Berrill, J.B., 'Energy Dissipation and Liquefaction at Port Island, Kobe', *Bull. NZ Nat. Soc. Earthq. Engg.*, **31**, 31-50 (1998).

19. Elgamal, A.W. and Zeghal, M., 'Liquefaction of reclaimed land in Kobe, Japan', *Jour. Geotech Engg.*, ASCE, **122**, 39-49 (1996).

20. Kazama, M., 'Nonlinear dynamic behaviour of the ground inferred from strong motion array records at Kobe Port Island during the 1995 Hyogo-ken Nambu earthquake', *Proc. Int. Workshop Site Response*, Port and Harbour Research Institute, **2**, 185-199, January 1996.

21. Wen, K.-L., and Yeh, Y.T., 'Seismic velocity structure beneath the SMART 1 array', *Bull. Inst. Earth Sciences*, Academia Sinica, **4**, 51-72 (1984).

22. Abrahamson, N.A., Bolt, B.A., Darragh,R.B., Penzien, J., and Tsai, Y.B., 'The SMART 1 accelerograph array (1981-1987), a review', *Earthquake Spectra*, **3**, 263-287 (1987).

23. Beresnev, I.A., Wen, K.-L., and Yeh, Y.T., 'Source, path and site effects on dominant frequency and spatial variation of strong ground motion recorded by SMART 1 and SMART 2 arrays in Taiwan', *Earthquake Engg. Struct. Dyns.*, **23**, 583-597 (1994).

24. Hushmand, B., Scott, R.F., and Crouse, C.B. ,"In-place calibration of USGS transducers at Wildlife liquefaction site, California, USA." *Proc. 10th World Conf. On Earthquake Engg.*, A.A.Balkema, Rotterdam, 1263-1268, (1992).

25. Youd, T.L. and Holtzer, T.L. ,"Piezometer performance at Wildlife Liquefaction Site, California." *Jour. Geotech. Engg.*, ASCE, **120**, pp.975-995 (1994).

26. Zeghal, M., and Elgamal, A.W. ,"Analysis of site liquefaction using earthquake records." *J. Geotech. Engg.*, ASCE, **120**, 996-1017 (1994).

27. Dobry, R., Ladd, R.S., Yokel, F.Y., Chung, R.M., and Powell, D. "Prediction of pore water pressure buildup and liquefaction of sands during earthquakes by the cyclic strain method." *NBS Building Science Series 138*, National Bureau of Standards, 150pp (1982).

28. Archuleta, R.J. ,"Direct observation of nonlinearity in accelerograms." *Proc. 2nd Int. Symp. Effects of Surface Geology on Seismic Motion*, eds. K. Irikura, K. Kudo, H. Okada and T. Sasatani, A.A Balkema, pp.787-792 (1998).

29. Holtzer, T.L., Private communication, 1999.

APPENDIX

Below is shown a FORTRAN listing of the one of the programmes used to synthesise shear stress and strain from measured downhole acceleration records. A suite of programmes was developed to consider the various numbers of downhole instruments and soils layers. The listing shown here is a typical example.

```
C   4KAPL22.FOR - FOURIER APPROXIMATION
C          OF STRESS AND STRAIN AT DEPTH H
C          BASED ON FOUR INSTRUMENTS
C
C      LAYERED SOIL PROFILE: TWO LAYERS OVER HALFSPACE.
C
C   NOTE: THIS VERSION IS SPECIFICALLY FOR CALCULATION OF
C        STRESSES AND STRAINS IN LAYER 2 ONLY.
C
C      BOTH E-W AND N-S RECORDS ARE USED
C
C      HERE DA, DB, DC AND DD ARE THE FOUR DISPLACEMENT RECORDS
C      FROM DEPTHS HA, HB, HC AND HD, MEASURED FROM THE UPPER
c      LAYER SURFACE. THE LAYER THICKNESSES ARE
C      H1, H2, WHILE THE SHEAR VELOCITIES OF THE LAYERS
C      ARE C1, C2, C3. OMEGA IS THE FREQUENCY OF EXCITATION
C      AND AK1, AK2, AND AK3 ARE THE CORRESPONDING WAVE NUMBERS.
C
C      H IS THE DEPTH AT WHICH THE STRAIN AND STRESS ARE APPROXIMATED.
C
    DATA RHO /1.80/
    OPEN(8,FILE='PROFILE4.DAT',STATUS='OLD')
    READ(8,*)HA,HB,HC,HD
    READ(8,*)LAYERA,LAYERB,LAYERC,LAYERD
    READ(8,*)C1,C2,C3
    READ(8,*)H1,H2
    WRITE(6,*)'   HA          HB          HC          HD'
    WRITE(6,*)HA,HB,HC,HD
    WRITE(6,*)' '
    WRITE(6,*)'   C1          C2          C3'
    WRITE(6,*)C1,C2,C3
    WRITE(6,*)' '
    WRITE(6,*)'   H1          H2'
    WRITE(6,*)H1,H2
    WRITE(6,*)' '
    OPEN(2,FILE='KDAT2.DAT',STATUS='OLD')
C
C   KDAT2.DAT CONTAINS THE DOWNHOLE RECORDS IN THE ORDER:
C
C   TIME
C   E-W ACCELERATIONS FOR DEPTHS A,B,C,D
C   E-W DISPLACEMENTS FOR DEPTHS A,B,C,D
C   N-S ACCELERATIONS FOR DEPTHS A,B,C,D
C   N-S DISPLACEMENTS FOR DEPTHS A,B,C,D
C
    WRITE(6,*)'ENTER FREQUENCY OMEGA AND DEPTH H'
    WRITE(6,*)'*** NOTE THAT H IS MEASURED FROM THE UPPER SURFACE'
```

```
      WRITE(6,*)'   OF LAYER 2 AND CANNOT EXCEED',H2
      READ(5,*)OMEGA,H
      AK1=OMEGA/C1
      AK2=OMEGA/C2
      AK3=OMEGA/C3
      OPEN(3,FILE='SSL4.DAT',STATUS='NEW')
C
      C1A=COEF(1,H1,H2,HA,C1,C2,C3,OMEGA,LAYERA)
      C2A=COEF(2,H1,H2,HA,C1,C2,C3,OMEGA,LAYERA)
      C3A=COEF(3,H1,H2,HA,C1,C2,C3,OMEGA,LAYERA)
      C4A=COEF(4,H1,H2,HA,C1,C2,C3,OMEGA,LAYERA)
      C1B=COEF(1,H1,H2,HB,C1,C2,C3,OMEGA,LAYERB)
      C2B=COEF(2,H1,H2,HB,C1,C2,C3,OMEGA,LAYERB)
      C3B=COEF(3,H1,H2,HB,C1,C2,C3,OMEGA,LAYERB)
      C4B=COEF(4,H1,H2,HB,C1,C2,C3,OMEGA,LAYERB)
      C1C=COEF(1,H1,H2,HC,C1,C2,C3,OMEGA,LAYERC)
      C2C=COEF(2,H1,H2,HC,C1,C2,C3,OMEGA,LAYERC)
      C3C=COEF(3,H1,H2,HC,C1,C2,C3,OMEGA,LAYERC)
      C4C=COEF(4,H1,H2,HC,C1,C2,C3,OMEGA,LAYERC)
      C1D=COEF(1,H1,H2,HD,C1,C2,C3,OMEGA,LAYERD)
      C2D=COEF(2,H1,H2,HD,C1,C2,C3,OMEGA,LAYERD)
      C3D=COEF(3,H1,H2,HD,C1,C2,C3,OMEGA,LAYERD)
      C4D=COEF(4,H1,H2,HD,C1,C2,C3,OMEGA,LAYERD)
C
      DET =((C1B-C1A)*C2C+(C1A-C1C)*C2B+(C1C-C1B)*C2A)*C3D
     &  +((C1A-C1B)*C2D+(C1D-C1A)*C2B+(C1B-C1D)*C2A)*C3C
     &  +((C1C-C1A)*C2D+(C1A-C1D)*C2C+(C1D-C1C)*C2A)*C3B
     &  +((C1B-C1C)*C2D+(C1D-C1B)*C2C+(C1C-C1D)*C2B)*C3A
C
      DET1=((C1A*C2B-C1B*C2A)*C3C
     &   +(C1C*C2A-C1A*C2C)*C3B
     &   +(C1B*C2C-C1C*C2B)*C3A)*C4D+
C
     &   ((C1B*C2A-C1A*C2B)*C3D
     &   +(C1A*C2D-C1D*C2A)*C3B
     &   +(C1D*C2B-C1B*C2D)*C3A)*C4C+
C
     &   ((C1A*C2C-C1C*C2A)*C3D
     &   +(C1D*C2A-C1A*C2D)*C3C
     &   +(C1C*C2D-C1D*C2C)*C3A)*C4B+
C
     &   ((C1C*C2B-C1B*C2C)*C3D
     &   +(C1B*C2D-C1D*C2B)*C3C
     &   +(C1D*C2C-C1C*C2D)*C3B)*C4A
C
C   BUILD MINORS
C
      B0A=(C1B*C2C-C1C*C2B)*C3D
     &  +(C1D*C2B-C1B*C2D)*C3C
     &  +(C1C*C2D-C1D*C2C)*C3B
      B1A=(C2B-C2C)*C3D+(C2D-C2B)*C3C+(C2C-C2D)*C3B
      B2A=(C1C-C1B)*C3D+(C1B-C1D)*C3C+(C1D-C1C)*C3B
      B3A=(C1B-C1C)*C2D+(C1D-C1B)*C2C+(C1C-C1D)*C2B
C
      B0B=(C1C*C2A-C1A*C2C)*C3D
     &  +(C1A*C2D-C1D*C2A)*C3C
     &  +(C1D*C2C-C1C*C2D)*C3A
      B1B=(C2C-C2A)*C3D+(C2A-C2D)*C3C+(C2D-C2C)*C3A
      B2B=(C1A-C1C)*C3D+(C1D-C1A)*C3C+(C1C-C1D)*C3A
      B3B=(C1C-C1A)*C2D+(C1A-C1D)*C2C+(C1D-C1C)*C2A
```

```
C
      B0C=(C1A*C2B-C1B*C2A)*C3D
     & +(C1D*C2A-C1A*C2D)*C3B
     & +(C1B*C2D-C1D*C2B)*C3A
      B1C=(C2A-C2B)*C3D+(C2D-C2A)*C3B+(C2B-C2D)*C3A
      B2C=(C1B-C1A)*C3D+(C1A-C1D)*C3B+(C1D-C1B)*C3A
      B3C=(C1A-C1B)*C2D+(C1D-C1A)*C2B+(C1B-C1D)*C2A
C
      B0D=(C1B*C2A-C1A*C2B)*C3C
     & +(C1A*C2C-C1C*C2A)*C3B
     & +(C1C*C2B-C1B*C2C)*C3A
      B1D=(C2B-C2A)*C3C+(C2A-C2C)*C3B+(C2C-C2B)*C3A
      B2D=(C1A-C1B)*C3C+(C1C-C1A)*C3B+(C1B-C1C)*C3A
      B3D=(C1B-C1A)*C2C+(C1A-C1C)*C2B+(C1C-C1B)*C2A
C
      A1A=(C2B*C3C-C2C*C3B)*C4D
     & +(C2D*C3B-C2B*C3D)*C4C
     & +(C2C*C3D-C2D*C3C)*C4B
      A2A=(C1C*C3B-C1B*C3C)*C4D
     & +(C1B*C3D-C1D*C3B)*C4C
     & +(C1D*C3C-C1C*C3D)*C4B
      A3A=(C1B*C2C-C1C*C2B)*C4D
     & +(C1D*C2B-C1B*C2D)*C4C
     & +(C1C*C2D-C1D*C2C)*C4B
      A4A=(C1C*C2B-C1B*C2C)*C3D
     & +(C1B*C2D-C1D*C2B)*C3C
     & +(C1D*C2C-C1C*C2D)*C3B
C
      A1B=(C2C*C3A-C2A*C3C)*C4D
     & +(C2A*C3D-C2D*C3A)*C4C
     & +(C2D*C3C-C2C*C3D)*C4A
      A2B=(C1A*C3C-C1C*C3A)*C4D
     & +(C1D*C3A-C1A*C3D)*C4C
     & +(C1C*C3D-C1D*C3C)*C4A
      A3B=(C1C*C2A-C1A*C2C)*C4D
     & +(C1A*C2D-C1D*C2A)*C4C
     & +(C1D*C2C-C1C*C2D)*C4A
      A4B=(C1A*C2C-C1C*C2A)*C3D
     & +(C1D*C2A-C1A*C2D)*C3C
     & +(C1C*C2D-C1D*C2C)*C3A
C
      A1C=(C2A*C3B-C2B*C3A)*C4D
     & +(C2D*C3A-C2A*C3D)*C4B
     & +(C2B*C3D-C2D*C3B)*C4A
      A2C=(C1B*C3A-C1A*C3B)*C4D
     & +(C1A*C3D-C1D*C3A)*C4B
     & +(C1D*C3B-C1B*C3D)*C4A
      A3C=(C1A*C2B-C1B*C2A)*C4D
     & +(C1D*C2A-C1A*C2D)*C4B
     & +(C1B*C2D-C1D*C2B)*C4A
      A4C=(C1B*C2A-C1A*C2B)*C3D
     & +(C1A*C2D-C1D*C2A)*C3B
     & +(C1D*C2B-C1B*C2D)*C3A
C
      A1D=(C2B*C3A-C2A*C3B)*C4C
     & +(C2A*C3C-C2C*C3A)*C4B
     & +(C2C*C3B-C2B*C3C)*C4A
      A2D=(C1A*C3B-C1B*C3A)*C4C
     & +(C1C*C3A-C1A*C3C)*C4B
     & +(C1B*C3C-C1C*C3B)*C4A
```

```
      A3D=(C1B*C2A-C1A*C2B)*C4C
     & +(C1A*C2C-C1C*C2A)*C4B
     & +(C1C*C2B-C1B*C2C)*C4A
      A4D=(C1A*C2B-C1B*C2A)*C3C
     & +(C1C*C2A-C1A*C2C)*C3B
     & +(C1B*C2C-C1C*C2B)*C3A
C
      S12H=COS(AK1*H1)*SIN(AK2*H)+(C1/C2)*SIN(AK1*H1)*COS(AK2*H)
      S22H=COS(2.*AK1*H1)*SIN(2.*AK2*H)
     & +(C1/C2)*SIN(2.*AK1*H1)*COS(2.*AK2*H)
      S32H=COS(3.*AK1*H1)*SIN(3.*AK2*H)
     & +(C1/C2)*SIN(3.*AK1*H1)*COS(3.*AK2*H)
      S42H=COS(4.*AK1*H1)*SIN(4.*AK2*H)
     & +(C1/C2)*SIN(4.*AK1*H1)*COS(4.*AK2*H)
C
      BIGBA=S12H*B1A+2.*S22H*B2A+3.*S32H*B3A
      BIGBB=S12H*B1B+2.*S22H*B2B+3.*S32H*B3B
      BIGBC=S12H*B1C+2.*S22H*B2C+3.*S32H*B3C
      BIGBD=S12H*B1D+2.*S22H*B2D+3.*S32H*B3D
C
      P12H=RHO*(COS(AK1*H1)*SIN(AK2*H)
     & -(C1/C2)*SIN(AK1*H1)*(1.-COS(AK2*H)))/AK2
      P22H=RHO*(COS(2.*AK1*H1)*SIN(2.*AK2*H)
     & -(C1/C2)*SIN(2.*AK1*H1)*(1.-COS(2.*AK2*H)))/(2.*AK2)
      P32H=RHO*(COS(3.*AK1*H1)*SIN(3.*AK2*H)
     & -(C1/C2)*SIN(3.*AK1*H1)*(1.-COS(3.*AK2*H)))/(3.*AK2)
      P42H=RHO*(COS(4.*AK1*H1)*SIN(4.*AK2*H)
     & -(C1/C2)*SIN(4.*AK1*H1)*(1.-COS(4.*AK2*H)))/(4.*AK2)
C
      BIGAA=P12H*A1A+P22H*A2A+P32H*A3A+P42H*A4A
      BIGAB=P12H*A1B+P22H*A2B+P32H*A3B+P42H*A4B
      BIGAC=P12H*A1C+P22H*A2C+P32H*A3C+P42H*A4C
      BIGAD=P12H*A1D+P22H*A2D+P32H*A3D+P42H*A4D
C
C   HERE FIND STRESS AT TOP OF LAYER 2
C
      S11H=SIN(AK1*H1)
      S21H=SIN(2.*AK1*H1)
      S31H=SIN(3.*AK1*H1)
      S41H=SIN(4.*AK1*H1)
C
      BLITAA=S11H*A1A+S21H*A2A/2.+S31H*A3A/3.+S41H*A4A/4.
      BLITAB=S11H*A1B+S21H*A2B/2.+S31H*A3B/3.+S41H*A4B/4.
      BLITAC=S11H*A1C+S21H*A2C/2.+S31H*A3C/3.+S41H*A4C/4.
      BLITAD=S11H*A1D+S21H*A2D/2.+S31H*A3D/3.+S41H*A4D/4.
C
 10   READ(2,*,END=999)T,AEA,AEB,AEC,AED,DEA,DEB,DEC,DED,
     &            ANA,ANB,ANC,AND,DNA,DNB,DNC,DND
C
C   E-W STRESS AND STRAIN APPROXIMATIONS
C
      TAUE=RHO*(BLITAA*AEA+BLITAB*AEB+BLITAC*AEC+BLITAD*AED)/AK1/DET1
      STRE=(BIGAA*AEA+BIGAB*AEB+BIGAC*AEC+BIGAD*AED)/DET1+TAUE
      GAMMAE=-AK1*(BIGBA*DEA+BIGBB*DEB+BIGBC*DEC+BIGBD*DED)/DET
C
C   N-S STRESS AND STRAIN APPROXIMATIONS
C
      TAUN=RHO*(BLITAA*ANA+BLITAB*ANB+BLITAC*ANC+BLITAD*AND)/AK1/DET1
      STRN=(BIGAA*ANA+BIGAB*ANB+BIGAC*ANC+BIGAD*AND)/DET1+TAUN
      GAMMAN=-AK1*(BIGBA*DNA+BIGBB*DNB+BIGBC*DNC+BIGBD*DND)/DET
```

```
C
      WRITE(3,199)T,STRE,GAMMAE,STRN,GAMMAN
 199  FORMAT(F8.3,6E12.4)
      GO TO 10
C
 999  STOP
      END
C
      FUNCTION COEF(I,H1,H2,H,C1,C2,C3,OMEGA,LAYER)
      AK1=I*OMEGA/C1
      AK2=I*OMEGA/C2
      AK3=I*OMEGA/C3
      GO TO (10,20,30)LAYER
 10   COEF=COS(AK1*H)
      RETURN
C
 20   COEF=COS(AK1*H1)*COS(AK2*H)-(C1/C2)*SIN(AK1*H1)*SIN(AK2*H)
      RETURN
C
 30   COEF=COS(AK1*H1)*COS(AK2*H2)*COS(AK3*H)
     &  -(C1/C2)*(SIN(AK1*H1)*SIN(AK2*H2)*COS(AK3*H))
     &  -(C2/C3)*(COS(AK1*H1)*SIN(AK2*H2)*SIN(AK3*H))
     &  -(C1/C3)*(SIN(AK1*H1)*COS(AK2*H2)*SIN(AK3*H))
      RETURN
      END
```